

A Unified Framework for Harnessing Heat and Light with Hydrovoltaic Devices

Tarique Anwar¹ and Giulia Tagliabue^{1*}

¹*Laboratory of Nanoscience for Energy Technologies (LNET), STI, École Polytechnique Fédérale de Lausanne (EPFL), Lausanne 1015, Switzerland*

*To whom correspondence should be addressed: E-mail: giulia.tagliabue@epfl.ch

The conversion of ambient heat into electricity through natural evaporation presents a promising avenue for sustainable energy technologies. This study introduces a unified framework for evaporation-driven hydrovoltaic (EDHV) devices that transcends traditional mechanisms focused solely on ion streaming at the solid-liquid interface. Our approach harnesses both thermodiffusion and photovoltaic effects to effectively transform waste heat and solar energy into electrical power. Utilizing a top-evaporating surface paired with a bottom silicon-dielectric (core-shell) nanopillar array separated by a liquid layer, we demonstrate significant enhancements in power output under external heating and solar illumination. Our findings reveal that in addition to the movement of a polar solvent (like water and ethanol) and ions in a narrow, partially wetted region of the top electrode, thermally and light-assisted ion migration from the bottom to the top electrode plays a pivotal role in electricity generation. We developed an equivalent electrical circuit model that quantifies the latter contribution through the capacitive element denoted as transfer capacitance. We demonstrate a state-of-the-art open circuit voltage of 1V and output power density of 0.25W/m² at 0.1M concentration. Furthermore, we highlight the critical influence of material selection on device performance; transitioning from TiO₂ to Al₂O₃ dielectric shell results in voltage (power) enhancements of 1.9 (3.6 times) at 25°C and 1.6 (2.4 times) at 70°C. Notably, high silicon doping yields a 28% increase in open-circuit voltage and a 1.6-fold improvement in power output compared to low-doped samples. These results provide insights into advancing EDHV devices and suggest broader operational strategies that consider environmental conditions, water salinity, and material engineering to optimize the utilization of waste heat and sunlight.

1. Introduction

Evaporation, a natural process with an average global energy flux of 80 (W/m²)¹, has significant potential for energy harvesting. Hydrovoltaic technology, which generates energy through the direct interaction of materials with water²⁻⁴, has indeed emerged as a promising avenue for

sustainable energy generation⁵⁻⁸. Among these, evaporation-induced hydrovoltaic devices stand out due to their ability to operate without external mechanical energy input. This functionality is achieved through the synergy of spontaneous capillary action and evaporation, enabling autonomous, low-intensity energy supply solutions ideal for portable devices and Internet of Things applications⁹⁻¹¹. Moreover, they offer exciting possibilities for harvesting energy from low-grade waste heat (below 100°C) produced by industrial, agricultural, and domestic processes^{12,13}. Additionally, when integrated with solar-driven evaporators that leverage photothermal effects¹⁴, evaporation-driven hydrovoltaic (EDHV) devices can convert solar energy into electrical power, further enhancing their potential as a sustainable and renewable energy source. However, as device demonstrations and applications expand to include a broader range of materials and architectures, a debate persists regarding the fundamental mechanisms, optimal micro/nanostructures, and operating conditions of EDHV devices.

In recent years, EDHV devices utilizing micro-nanoporous materials have garnered significant attention for their ability to harness energy through the movement of electrolytes within partially wetted regions^{2,15,16}. This phenomenon, which occurs ahead of a liquid meniscus, facilitates the electrokinetic streaming of ions. Previous studies have identified several contributing phenomena, including the streaming potential^{4,6,17}, ionovoltic effect^{15,16,18}, and evaporating potential². Central to these mechanisms is the critical role of directional electrolyte flow near the liquid-solid interface. Additionally, going beyond the intricate micro- and nanostructures of typical EDHV devices^{4,17,19,20}, we recently utilized a controlled array of silicon nanopillars to demonstrate the significant impact of the geometrical and interfacial chemical properties of the nanostructures, particularly the role of the chemical equilibrium of the surface groups in enabling high salinity operation⁶, challenging the reliance of deionized water for high performance²¹. Furthermore, recent work introduced a passive hydrovoltaic device characterized by a limited evaporation rate and fluid permeation, capable of producing electricity through upstream proton diffusion²². This proton diffusion arises from the chemical potential difference between the wet and dry sides of the material, resulting in sustained electricity generation owing to the gradual permeation of water. Despite these advancements, it remains unclear how the various mechanisms identified in different nanomaterials and device geometries can be effectively

integrated into hydrovoltaic systems²⁰, or how to design structures that harness them simultaneously. Similarly, previous studies have indicated that combining light and heat can synergistically improve hydrovoltaic performance through enhanced photothermal evaporation^{7,23}. On the other hand, in nanofluidic systems with charged interfaces, thermo-osmotic flows can convert thermal gradients into electrical currents^{24,25}. However, one vital area remains largely overlooked: *how photocharging and photothermal effects contribute to ion migration*, which is a key process for the performance of hydrovoltaic devices⁶. This lack of understanding emphasizes the importance of a systematic study of light- and heat-driven ion dynamics, potentially revealing new methods to boost hydrovoltaic efficacy.

This work demonstrates a unified concept for EDHV devices that transcends traditional mechanisms focused solely on ion streaming at the solid-liquid interface. By employing a top-evaporating surface and a uniformly structured cm-scale bottom silicon-dielectric (core-shell) nanopillar array (Si NPs, see **Figure 1A**), we report major improvements in power output under external heating and solar illumination due to ion thermodiffusion in the electrolyte layer and photovoltaic effects at the solid/liquid interface. By using a combination of experiments, numerical calculations, and theoretical modeling, we reveal a mechanism where thermally and light-assisted ion migration plays a pivotal role in electricity generation, achieving a state-of-the-art open-circuit voltage of 1V and an output power density of 0.25W/m² at optimal conditions with 0.1M concentrations. Overall, our EDHV architecture transforms waste heat and solar energy into electrical power, surpassing prior photothermal evaporation schemes, by decoupling the top evaporating surface from the bottom nanostructure opens a completely new design space for these systems, ultimately paving the way for more efficient utilization of renewable energy sources.

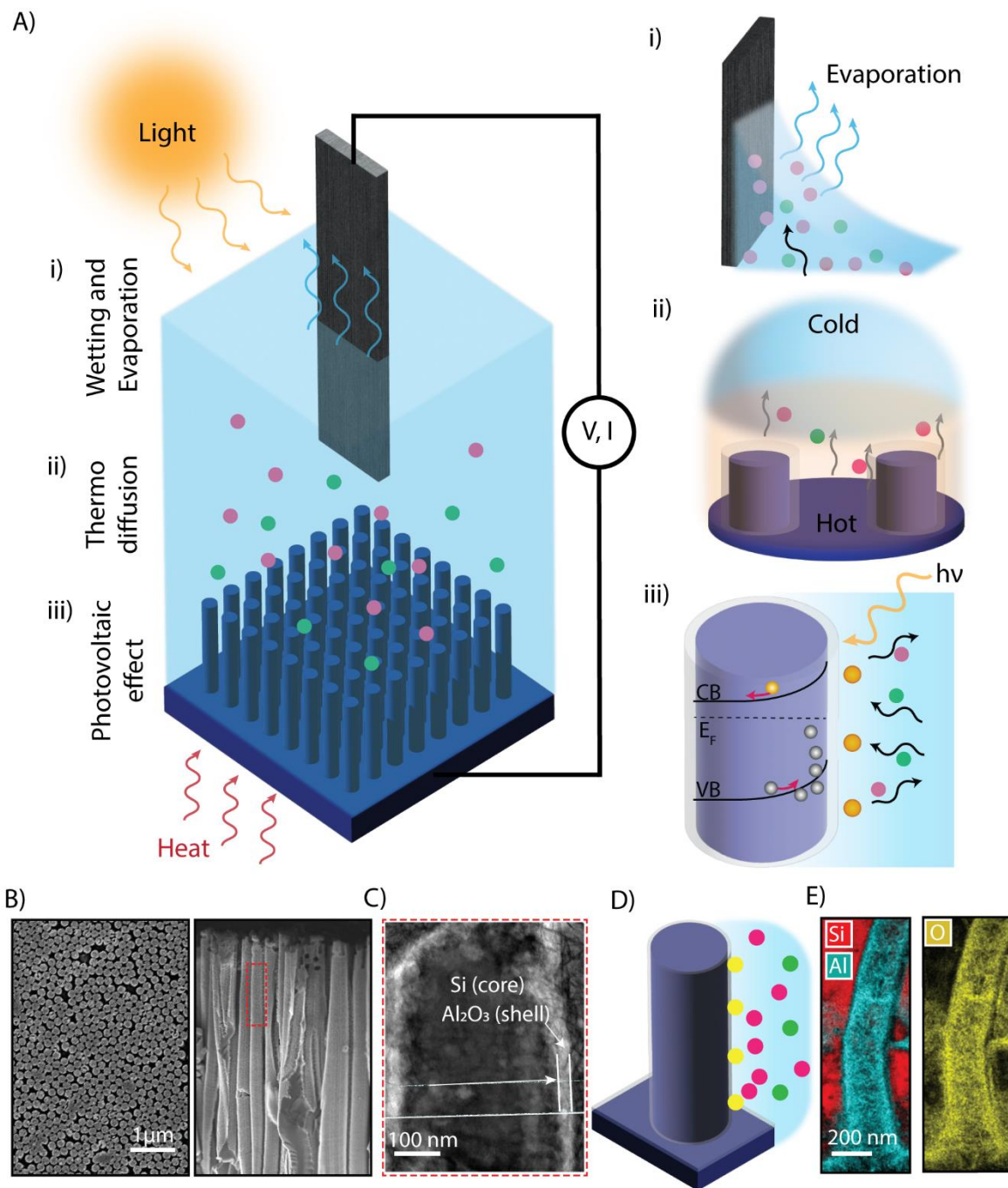


Figure 1: Evaporation-driven Hydrovoltaic Device Architecture, Mechanisms, and Materials. A) Schematic representation of the hydrovoltaic device featuring a top evaporating electrode surface and a bottom array of SiNPs immersed in water. The top and bottom components do not physically contact but are electrochemically connected through the water. The inset displays the three effects contributing to the device's performance. i) A side view of the evaporating surface with the liquid meniscus. ii) Intermediate electrolyte layer and chemical equilibrium at the bottom nanostructures. iii) photoactive nanostructure-electrolyte interface. B) Scanning electron microscopy (SEM) image of the SiNPs array. (left) Top view, and (right) cross-sectional view. C) Scanning tunneling electron microscopy (STEM) image of a single NP. The cross-sectional cut of a single NP reveals the presence of a silicon core and Al_2O_3 shell. D) A single NP composed of silicon (core) and an Al_2O_3 shell exhibits surface charge at the liquid-solid interface, with a more detailed view of the interface, highlighting the charged surface and the resulting electrical double layer. E) TEM-EDX image of the NP displaying the elemental maps of the aluminum, silicon, and oxygen.

2. Results

Understanding the fundamental mechanisms of voltage and current generation in EDHV devices requires control over the solid-liquid interface properties. Our devices feature a bottom cm-scale regular array of Si NPs (**Figure 1A**), fabricated using a combination of Nanosphere lithography and metal-assisted chemical etching of a Si wafer (see **Methods**, **Figure 1B**). To passivate the surface, we use atomic-layer deposition to coat the Si/SiO₂ core, where SiO₂ is the native oxide layer, with dielectric shells of Al₂O₃ or TiO₂ (see **Figure 1C** and **1D**). For hydrovoltaic testing, the sample is placed inside a custom HV cell and wetted with 250 μ l of deionized water containing KCl salt of varying concentrations (from 10 μ M to 0.1 M). Already in ambient conditions (T = 22-24°C and humidity = 25-30%), evaporation occurs naturally (**Figure S1**). Our testing HV cell is uniquely designed to prevent contact between the solution and the bottom (Aluminum) electrode, which could lead to unwanted chemical reactions, and to ensure that only the central part of the silicon ($\sim 1\text{cm}^2$ area) is in contact with the electrolyte (**Figure S2**). Next, the HV cell is positioned on a microbalance to track the evaporation rate. The electrical response is measured using a top Ag/AgCl or graphite electrode (**Figure S3**), placed in the liquid right above the Si NPs, and an aluminum contact previously deposited on the back surface of the Si wafer (**Figure 1A** and **Methods**). During the electrical measurements, the top electrode and bottom silicon substrate are decoupled, and the electrical circuit is complete as soon as the liquid is dispensed; thereafter, voltage and current can be measured. Heat and light stimuli are applied using a Peltier cell and a Xenon lamp, respectively, while measuring the open circuit voltage, V_{OC} , or power output of the device under different temperatures and irradiation (see **Methods**).

Figure 1D shows a zoom-in view of a single NP within our device. Upon wetting, the oxide layer on the surface of the Si NPs (**Figure 1E**) dissociates, resulting in a net negative surface charge σ (yellow circles). Concurrently, positive ions adsorb on the surface (pink circles), and an electrical double layer (EDL) develops within the liquid²⁶. Any resulting imbalance in the ion distribution along the NP length contributes to the measured electrical potential difference. Interestingly, we observe that, due to the closed bottom surface of the nanochannel, the studied geometry presents an intrinsic asymmetry in the surface-charge distribution. As a result, even in the absence of an evaporation-induced flow, a chemical potential difference exists, and therefore, a

V_{OC} can be measured between the top electrode and the bottom SiNPs surface⁶. The V_{OC} and the power curves of the device were recorded as a function of the physical and chemical properties of the system under varying conditions of temperature and light irradiation (see **Methods**), which will be discussed extensively in the following sections.

2.1 Role of Temperature.

We first conducted a series of experiments explicitly analyzing the open circuit voltage generated at different temperatures of the bottom SiNPs electrode, denoted as T_S . To trigger the temperature changes, we utilized an external Peltier heater placed beneath the SiNPs electrode. Concurrently, we monitored the temperatures using an infrared camera positioned above the sample.

Figure 2A provides a time trace of the open circuit voltage of a SiNPs device with N-type low-doping silicon core nanopillars coated with Al_2O_3 . At the beginning of the experiment (dry sample), the voltage was zero. As soon as the electrolyte wets the sample, we observe a gradual increase in voltage until a steady-state value is reached (0.25V). When we activate the heater (at 125 s), the voltage experiences a noticeable rise, eventually approaching twice the initial value (0.5 V). The corresponding time-trace for T_S , as recorded by the infrared camera, is depicted in **Figure 2B** (empty symbols). As the heater operates, the temperature steadily climbs and ultimately stabilizes around 70 °C for the maximum power applied to the heater. Once the heater is turned off, we observe an immediate drop in temperature and V_{OC} . Notably, the cooling rate is slower than the heating phase, which can be attributed to restricted pathways for heat dissipation.

It is important to highlight that the temperature of the top electrode, located at the air-water interface, is lower than the measured T_S due to the cooling effect of evaporation and the differing thermal environments present at the bottom (heating source) and top (ambient air) of the setup. We quantified this temperature difference as ΔT . **Figure 2B** illustrates the time trace of ΔT as T_S is increased from the ambient temperature of 25 °C to 70 °C, peaking at around 7 K (see **supplementary information S4** for details on temperature measurements).

Lastly, we explored how different surface properties affect the device's open circuit performance metrics in relation to T_S . **Figure 2C** presents the voltage-temperature profile for two distinct samples that share the same silicon N-type low doping core but differ in their outer shells, composed of Al_2O_3 (pink curves) and TiO_2 (green curves), respectively. This analysis was conducted at two concentrations of KCl, specifically 1 mM and 100 mM, providing valuable insights into the device's behavior under varying electrolyte conditions.

Our results indicate that, up to a temperature rise of 20 K, the voltage exhibited a linear relationship with temperature across all experimental conditions, although with different slopes. As shown in **Figure 2E**, the slopes are consistently higher for samples of Al_2O_3 shells (pink curves) than TiO_2 (green curves). However, as the temperature rises beyond this threshold, we observe a transition to a non-linear increase in voltage. Overall, we observed that temperature directly affects the chemical equilibrium at the solid-liquid interface, increasing surface charge and V_{OC} linearly within a limited range. The surface nature is crucial in this relationship, but temperature also leads to a non-linear increase in V_{OC} , which requires further analysis, and thus will be discussed in **section 3**.

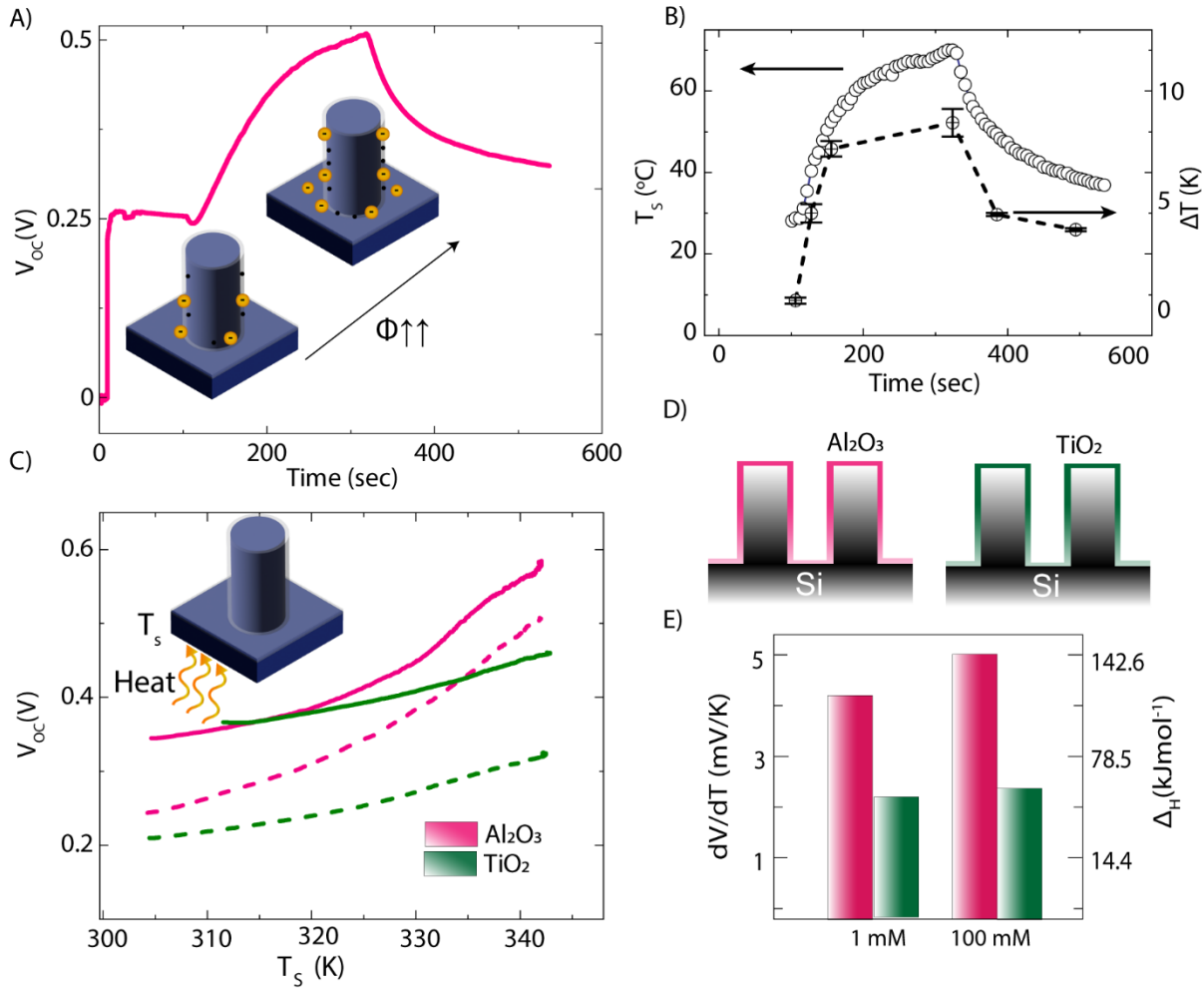


Figure 2: Role of Temperature for different coatings and salinity levels. A) The time trace of the measured open circuit voltage at ambient temperature is presented when the silicon surface temperature is increased and then allowed to cool down. The inset illustrates a qualitative rise in the chemical potential difference for a single NP that has been wetted with electrolyte. B) The time trace of the silicon surface temperature when the heater is turned on and turned off once the maximum is reached. The right axis shows the corresponding temperature difference between the bottom silicon surface and the top electrode (at the end of the liquid meniscus). C) The voltage-temperature profile of the two devices was measured using the same top electrode at varying salinities. Each device consists of an identical silicon core and a dielectric shell made of Al₂O₃ and TiO₂: 1 mM (solid lines) and 100 mM (dashed lines). D) Schematic representation of the core-shell nanopillars with Al₂O₃ (pink) and TiO₂ (green) shells. E) The slope of the V_{oc} -temperature curves for the linear regime (up to a 20K increase in temperature) and the corresponding estimated values of ΔH .

2.2 Role of Light Irradiation.

Next, we conducted a comprehensive series of measurements to understand the device performance under various illumination conditions as a function of the solid and interfacial properties. We begin by assessing the open circuit voltage of the same samples of the temperature-dependent study, namely N-type low-doping silicon core nanopillars coated with

Al₂O₃ and TiO₂. The V_{OC} time trace is shown in **Figure 3A** (green for TiO₂ and pink for Al₂O₃), omitting the transient phase where it rises from 0 V to a steady state value for improved clarity.

Under ambient conditions, before illumination, the devices show a stable voltage (0.36 V Al₂O₃, 0.15 V TiO₂). Upon exposing the samples to solar illumination (AM 1.5, 1 kW/m²), we observed an instantaneous increase in the measured voltage, which quickly stabilized at a significantly higher steady-state value (0.55 V Al₂O₃, 0.33 V TiO₂). Conversely, when we turned off the light source, the voltage immediately decreased, reverting to its initial value recorded in the dark. To validate the consistency of this response, we performed multiple cycles of switching the light on and off, and each cycle demonstrated a reliable and pronounced rise and fall in voltage.

To relate the observed V_{OC} change with the properties of the solid-liquid interface, we measured the device's complex impedance in real time at a fixed frequency of 1 kHz. In fact, this methodology allowed us to quantify the time-dependent changes in capacitance, also reported in **Figure 3A** with open symbols. We found that upon illumination, the capacitance also experienced a sharp increase while it reverted to the initial value once the light was switched off, correlating well with the measured changes in V_{OC}.

We also measured the open circuit voltage of these two samples for a range of solar-light intensities (ranging from 0 to 1.4 kW/m²) and salinities (from 0.01 mM to 100 mM). As depicted in **Figure 3B**, the steady-state open circuit voltage exhibits an increase with rising solar intensity, although the relationship appears logarithmic-like in nature. Additionally, **Figure 3C** presents the photovoltage, defined as $V_{ph} = V_{OC}^{light} - V_{OC}^{dark}$, for both materials across varying salinities. Notably, our observations reveal that the photovoltage recorded for samples with Al₂O₃ shells consistently surpassed the TiO₂ samples, regardless of the salinity levels tested. Furthermore, the photovoltage displayed a minimal decrease with increasing salinity levels.

Finally, we expanded our open-circuit voltage testing to assess the role of silicon in the observed behavior. Specifically, we compared the response of three Al₂O₃ coated samples with different silicon doping, specifically Low N-doping (1-20 Ω.cm), High N-doping (<0.005 Ω.cm), and p-doping (0.1-0.5 Ω.cm). As already shown in **Figure 3A**, the low N-doped silicon core exhibits a significant voltage increase (>150 mV) under illumination, followed by a return to its initial value when the

light is turned off. The high N-doped silicon core samples displayed a similar but less pronounced response (**Figure S5**), with the light-induced change in voltage (+20 mV) being weaker than that seen in the low N-doped counterpart. In stark contrast, the P-doped silicon core manifested a decrease in voltage (-35 mV) upon illumination, rebounding to the original value once the light was turned off. This observation underscores a notable trend: for the same solid/liquid interface, the magnitude of light-induced voltage changes is inversely proportional to the doping concentration, irrespective of the doping type employed.

Overall, for a deeper understanding of the underlying mechanisms that contribute to these pronounced light-sensitive behaviors, we need to develop a more comprehensive model of the system, capable of capturing not only the solid-liquid interface but also the light response of the silicon core. In the following we introduce an equivalent circuit model and subsequently use it to gain a complete description of the device's behavior.

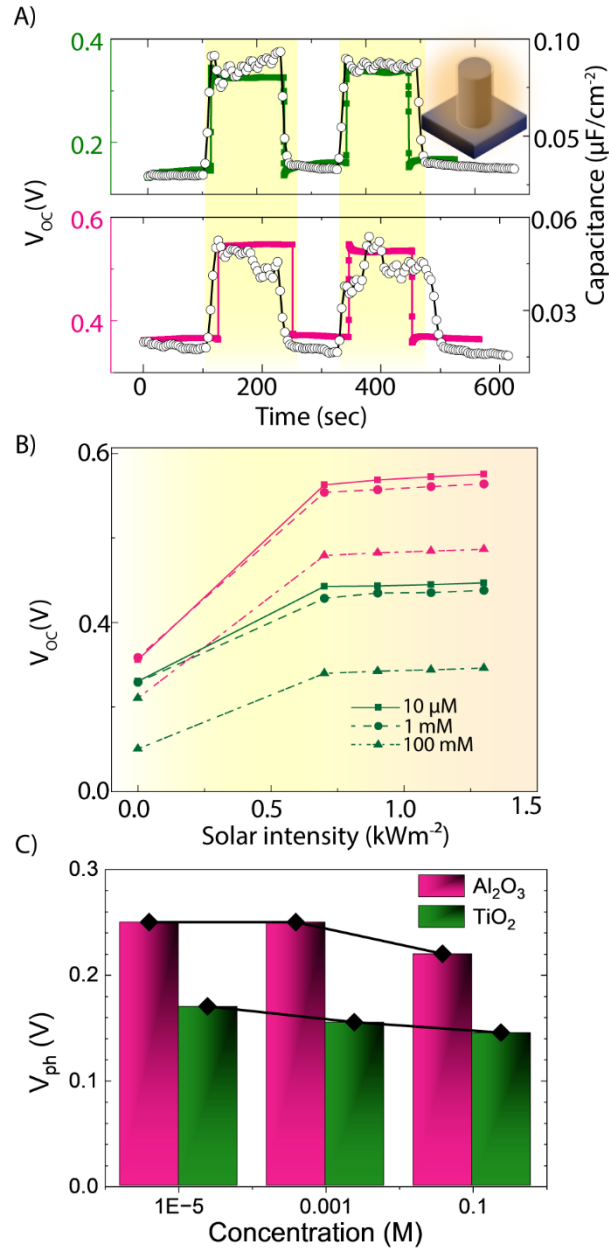


Figure 3: Role of Light for different coatings and salinity levels. A) Time trace of the measured open-circuit voltage and capacitance at 1 mM KCl for two devices with different dielectric shells. The test was conducted under ambient conditions and 1 Sun illumination (yellow-shaded region). B) Measurement of open circuit voltage under various solar intensities for two devices featuring different dielectric shells but identical silicon cores. 0.01 mM (solid lines), 1 mM (dashed lines), and 100 mM (dot-dashed lines). In all instances, pink and green colors correspond to devices with Al_2O_3 and TiO_2 shells, respectively; C) Measured photovoltage under 1 kW/m^2 intensity for samples with Al_2O_3 and TiO_2 shells (same low N-doped silicon core) at different concentrations of KCl.

2.3 Rationale for an Equivalent Electrical Circuit Model

As schematically illustrated in **Figure 4A**, we recognize that the studied system comprises three main components, namely the top electrode, the electrolyte layer, and the bottom nanostructured electrode, each with its solid/liquid interfaces. As discussed below, these components contribute to the device's behavior via evaporation-induced ion streaming, chemical potential difference, and photovoltage, respectively. Importantly, as the charges at the surface of each solid and the ion distribution in the electrolyte influence each other, any change in one of the three components affects the device's behavior in a complex manner. As we detail below, the equivalent circuit shown in **Figure 4B** represents well the device behavior. The analysis of the experimental results guided by the equivalent circuit model will be carried out in **Section 3**.

Evaporation-induced Ion Streaming at the Three-phase Boundary of the Top Electrode. As depicted within the green rectangle, the top electrode, which serves as the positive terminal for electrical measurements, is only partially immersed in the electrolyte, with the remaining portion exposed to air. This arrangement creates a liquid meniscus and a three-phase contact line around the perimeter of the electrode. The evaporation from this region generates fluid flow along the meniscus. The flow induced by evaporation drives ions in the liquid to stream, which can be represented by a current source, I_{evap} , with an appropriate resistance in parallel, named $R_{3\phi}$. Equivalently, it can also be represented by a voltage source with $R_{3\phi}$ in series (**Figure S6**). Physically, the voltage source originates due to the three-phase contact boundary that generates an evaporation-rate-dependent contact potential difference between the wet and dry sides of the top electrode²⁷.

Chemical Potential Gradient across the Electrolyte Layer: as illustrated in the yellow rectangle, the wetted portion of the top electrode and the bottom SiNPs have different surface charges, resulting in a chemical potential difference (Φ) across the electrolyte layer⁶. Due to this, the electrolyte region exhibits capacitive effects as the surface charges of either electrode are perturbed by thermal effects or light irradiation. We thus define a transfer capacitance C_{tr} of the electrolyte, which is the capacitance arising from ion transfer across it. The presence of a capacitive element in the system is further validated by fitting the V_{oc} time –trace of the device

using a single exponential with a characteristic RC time constant (**supplementary information S6**). On the other hand, Φ is quantified by **Eq. 1**, which depends on the temperature (T_S) and surface charge (σ) of the bottom silicon substrate:

$$\Phi = \frac{2k_B T_S}{e} \sinh^{-1} \left(\frac{\sigma}{\sqrt{8000 \epsilon_0 \epsilon_r c_0 k_B T_S}} \right) + \frac{\sigma}{C_{stern}} \quad (1)$$

The surface charge originates due to both electronic and ionic contributions. Firstly, thermal motion induces electron transfer between the solid's atoms and the water molecules, facilitated by overlapping of their electron clouds^{28,29}. Secondly, ionization reactions at the surface generate additional ions. For oxides-aqueous interfaces, such as Al_2O_3 , SiO_2 , and TiO_2 , in water, the surface dissociation can be described using the complexation model³⁰. For example, TiO_2 dissociates according to: $TiO_2 + H_2O \Leftrightarrow TiO^- + H_3O^+$. The above equilibrium reaction is governed by the equilibrium constant, which exhibits temperature dependencies as given by Eq. M8, resulting in increased surface charge (σ) and chemical potential difference as temperature increases.

Under equilibrium conditions, the chemical potential difference would cease to exist. However, due to the temperature gradient ΔT across the electrolyte layer, the non-zero chemical potential difference persists in the steady state. Overall, the yellow region can be modeled as a current source driven by the thermodiffusion, $I_{\Delta T}$, in parallel with a resistor, which accounts for the ionic resistance of the electrolyte solution R_{sol} , and a capacitor, C_{tr} .

Photovoltage at the Silicon-Oxide-Water Interface: to account for the influence of light, we need to examine the changes in interfacial band bending at the silicon-oxide-water interface as the sample is illuminated. As illustrated in **Figure 4D**, the generation of electron-hole pairs creates a quasi-Fermi level splitting that results in a photovoltage (V_{ph}), as shown in **Figure 3C**. This can be represented by a voltage source^{31,32} or, equivalently, by a current source, I_{ph} , in parallel with a resistance of the photoactive interfacial region (R_{Si}).

Based on the described equivalent electrical circuit, we can derive a few critical equations concerning the device response (full detail in **Methods**), which can be used to quantitatively analyze the experimental data and therefore clarify the response of this complex EDHV system.

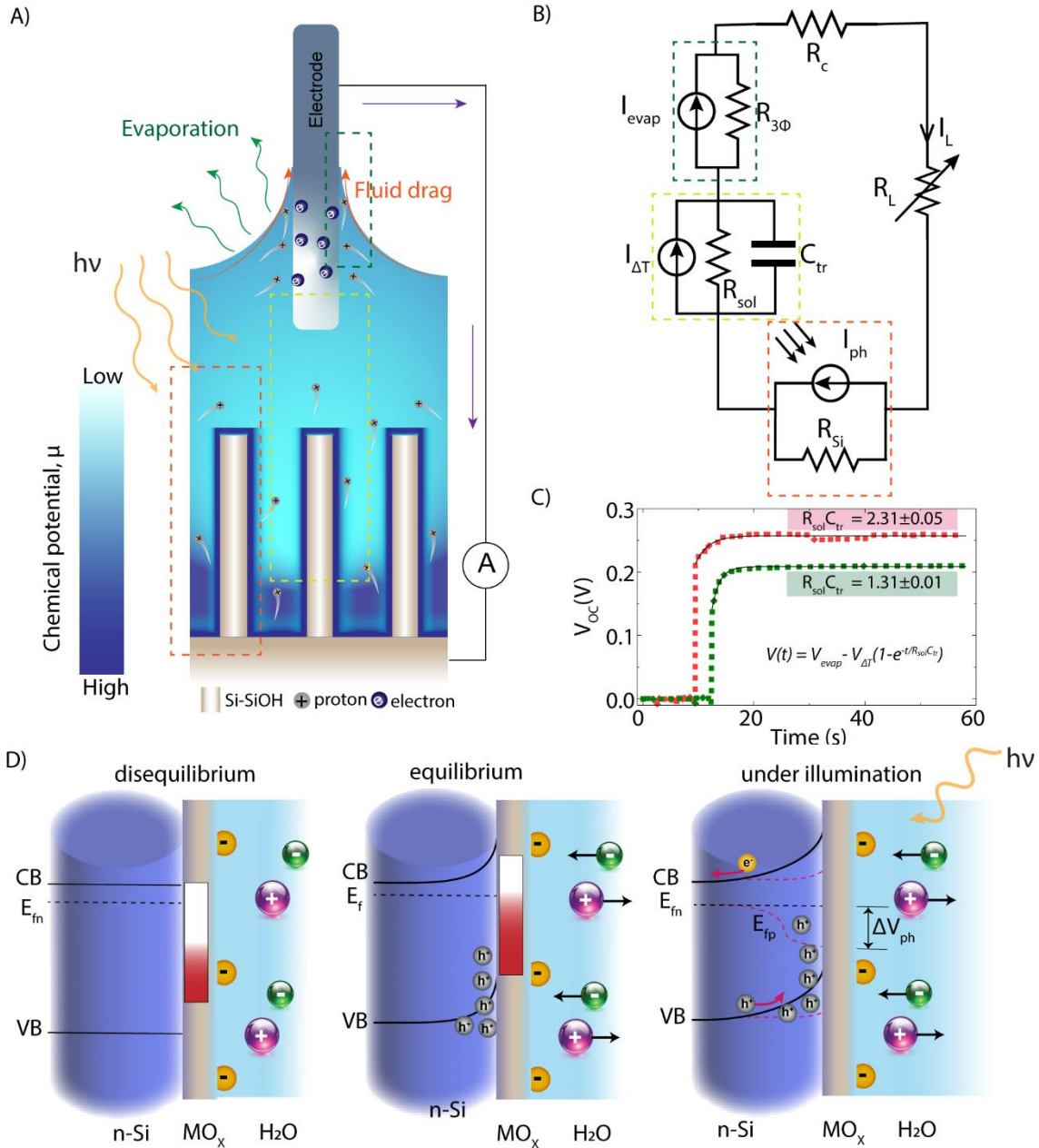


Figure 4: Equivalent Circuit Model of the EDHV Device. A) Schematic representation of the device working principle. The three regions enclosed in the box highlight the different aspects of the device that govern the electrical output. The green box illustrates the generation of a potential difference across the liquid wetting front caused by evaporation-driven fluid flow along the meniscus region. The yellow box depicts the existence of a chemical potential gradient (due to the differences in chemical characteristics of the surface and temperature) between the wetted parts of the top and bottom electrodes. The orange box shows the light-active region that generates photovoltage under solar illumination. B) An equivalent circuit representation of the device is outlined above. A contact resistance is included alongside a variable load resistance. C) Transient open circuit voltage (dotted lines) fitted using the derived equation (black solid lines). D) Band diagram of the semiconductor-metal oxide-electrolyte interface. (left) The liquid-solid interface is formed, but equilibrium has not yet been reached. (middle) Equilibrium has been established, resulting in Fermi-level alignment across the interface. (right) Under illumination, Fermi-level splitting occurs. The difference in the quasi-Fermi levels of electrons and holes equals the measured photovoltage.

3. Discussion

3.1 Influence of the top-electrode on the evaporation rate

To assess the role of the meniscus at the top electrode, we measured the evaporation rate from our working device with a 1 cm² area SiNP bottom electrode (Low N-doping, coated with Al₂O₃) under three different conditions: a) without any top electrode, b) with a W=0.8 mm (perimeter) top electrode, and c) with a W=3.2 mm top electrode. We observed that the evaporation rate nearly doubled when introducing the small electrode compared to the scenario without an electrode. Additionally, the evaporation rate increased nearly fourfold with the larger electrode, which correlates with the perimeter of the three-phase contact line (**Figure S1**).

We obtained an expression for the current source I_{evap} in the equivalent circuit (**Eq. M1**) that shows that it is indeed proportional to the evaporation velocity (v_f). This expression shows that I_{evap} depends on the surface charge ($\bar{\sigma}$) induced by the direct interaction of polar solvent molecules with the evaporating surface² as well as ion separation arising due to the chemical potential difference ($C_{tr}\Phi$) across the electrolyte. To confirm the involvement of the solvent in the process, we tested the device using water or ethanol under otherwise identical conditions. The measured V_{oc} values for DI water and ethanol at T_s equal to 25 °C (65 °C) are 0.552 V (0.690 V), and 0.195 V (0.336 V), respectively (**Figure S7**), confirming a clear dependence on the used solvent. Overall, these observations indicate the importance of ion streaming at the three-phase boundary created at the top electrode in the system and the need to include it explicitly in the equivalent circuit model.

3.2 Thermal Effects on the Open Circuit Voltage.

Using a previously validated COMSOL Multiphysics model⁶, which accounts for the liquid nanoconfinement and incorporates the temperature-dependent equilibrium constants for the oxide/liquid interface (see **Methods**), we calculated the electrostatic potential difference between the bulk electrolyte and bottom SiNPs as a function of temperature. We obtained a linear increase in potential difference with an increase in temperature up to 50 K above room temperature of 298 K (**Figure S8**). We further examined the slope of the voltage-temperature

curve (**Figure S8**) across various conditions, including pH, electrolyte concentration, and the initial equilibrium constant (K_{a0}), obtaining minimal dependence on these external factors. Indeed, the dV/dT slope is predominantly influenced by the enthalpy of dissociation of the surface groups, Δ_H , which is the chemical characteristic of the material. Based on the experimental results, Al_2O_3 displayed a more considerable voltage increase compared to TiO_2 for equivalent temperature rises (**Figure 2C**). Using this model to fit the linear part of the experimental V_{OC} - T_s curves (**Figure 2C**, up to 20K), we could then extract the value of Δ_H for each material and electrolyte concentration, showing that Al_2O_3 exhibits a higher Δ_H than TiO_2 (**Figure 2E**, right axis).

However, the experimental data shows that V_{OC} increases non-linearly when temperature rises more than 20K above ambient conditions. To elucidate the observed non-linear temperature dependence, we instead exploit the equivalent electrical circuit to determine the expression for V_{OC} (**Eq. 2**, see Methods), which includes the three contributions discussed in Section 2: (i) evaporation-induced ion streaming, (ii) the chemical potential difference, (iii) and photovoltage.

$$V_{OC} = v_f \bar{\sigma} r_{3\phi} + \Phi (1 + v_f r_{3\phi} C_{tr}) + V_{ph} \quad (2)$$

All quantities in the expression were defined previously. Notably, both Φ and v_f increase with temperature, thus their product in the second term leads to the observed quadratic dependence of the open circuit voltage on temperature (**Figure S9**).

As we mentioned above, from the transient response of the open circuit voltage (**Figure 4C**), it is possible to determine the RC time constant of the system and, hence, its transfer capacitance C_{tr} (**Supplementary Information S6**). Interestingly, assuming that variables like $v_f, \bar{\sigma}, r_{3\phi}$ depend on the top electrode but not on the bottom one, using the voltage-temperature traces in **Figure 2C** and the RC values for different conditions (1 mM or 100 mM salinities with Al_2O_3 or TiO_2 coatings), we determined the expression of $v_f r_{3\phi} / R_{sol}$ as a function of temperature for different electrolyte concentrations given by **Eq. S10.4** and displayed in **Figure S10 (Supplementary Information S10)** for detailed analysis). We indeed observe that this term increases with temperature. Thus, the temperature-dependent change in chemical equilibrium at the liquid-

solid interface and its role in facilitating ion migration contributes to a deeper understanding of the thermally induced dynamics of the presented system.

3.3 Light-induced potential change across the capacitive interface.

The presence of an oxide layer is crucial as it effectively passivates the silicon surface³³. This oxide layer plays a significant role in preventing chemical reactions between silicon and water, which would otherwise inhibit the generation of kinetic photovoltage³⁴. Even under conditions devoid of light, there is a notable increase in V_{OC} when the silicon core is passivated with aluminum oxide (Al_2O_3). This increase can be attributed to enhanced charge accumulation at the interface (**Figure S11**). This phenomenon of band bending at the silicon-oxide interface is primarily driven by surface states, which facilitate the equilibration of the Fermi level³⁵. Consequently, there is either electron or hole accumulation at the interface^{31,36}, leading to a net surface charge at the liquid-solid interface. If we denote the total number of surface sites as Γ and the concentration of protons at the liquid-solid interface as $[H^+]_S$, we can compute the surface charge using **Eq 3**:

$$\sigma = \frac{-e\Gamma}{1 + \frac{[H^+]_S}{K_a}} \quad (3)$$

When n-doped silicon is subjected to illumination, upward band bending occurs, accumulating holes at the silicon-oxide interface (**Figure 4D**). Simultaneously, on the liquid side, excess charges at the capacitive interface drive the dissociated cations of water, primarily hydronium ions (H_3O^+), away from the interface. It also creates an attractive force for hydroxide ions (OH^-), drawing them toward the interface to neutralize the accumulated holes. Consequently, this process leads to a reduction in the concentration of $[H^+]_S$ under illumination, increasing the surface charge (σ) that in turn produces a higher V_{OC} or a positive photovoltage (V_{ph}). Moreover, a differential capacitance, C_d , can be defined as the change in surface charge (σ) due to change Φ , and mathematically expressed as by $C_d = (\partial\Phi/\partial\sigma)^{-1}$, which increases with surface charge (see **supplementary information S12** for derivation). The observed increase in V_{OC} under illumination, which we have attributed to changes in the surface charge dynamics, is further corroborated by the alterations in capacitance, as evidenced in **Figure 3A**. In contrast, a decreasing open circuit voltage under illumination for p-type silicon can be linked to downward band bending arising

from electron accumulation at the interface (**Figure S5**). This subsequently drives protons toward the surface to neutralize the excess negative charge.

Our observations also reveal a slight increase in V_{OC} in high-doped n-type silicon (**Figure S5**), a phenomenon associated with a subtle shift in the quasi-Fermi level. To understand the relationship between the measured open circuit voltage and light intensity, we establish the dependence of Fermi level splitting on the incident solar intensity. Notably, the quantity of charge carriers generated is directly proportional to light intensity, expressed mathematically as $n_h \sim I_{solar}$. Conversely, the shift in the quasi-Fermi level for holes is tied to the hole concentration, represented as $n_h \sim \exp\left(-\frac{E_{fp}}{k_B T}\right)$. Consequently, we derive that the quasi-Fermi level E_{fp} and, therefore, the positive photovoltage (V_{ph}) can be expressed as approximately logarithmic in relation to solar intensity: $V_{ph} \sim \log(I_{solar})$, in agreement with the observed experimental trend (**Figure 3B**).

3.4 Power Output as a Function of Heat and Light.

Finally, we investigate the influence of various operational parameters on the power output of our device, emphasizing the effects of temperature, solar illumination, and electrolyte concentration. **Figure 5A** shows a schematic representation of power curve measurements by sweeping load resistances in the range 100 Ω -70k Ω . Firstly, the peak value (position) of the power curves increases (shift towards lower resistance) as the environmental conditions change from ambient ($T_s=25^\circ\text{C}$, no light irradiation) to 1 Sun ($T_s=25^\circ\text{C}$, 1kW/m² light irradiation) and then heat ($T_s=70^\circ\text{C}$, no light irradiation), as shown in **Figure 5B**. Notably, the measured power curves indicate that increasing the concentration of KCl from 1 mM to 100 mM nearly doubles the maximum power output despite a lower open circuit voltage at higher concentrations (note the different scales on the left and right y-axis). Furthermore, as observed in the power curves at varying temperatures (**Figure 5C**), the maximum power at 70 $^\circ\text{C}$ surpasses the ambient temperature output by over five times, demonstrating the profound impact of thermal conditions on device performance. Moreover, the parabolic dependence of power output and voltage (**Figure 5D**) across the load resistance underscores the importance of optimizing both aspects to achieve high performance.

The power output is governed by the equivalent electrical circuit, allowing us to derive an expression that captures the relationship between load resistance and output power. The simplification of this expression into a two-parameter family of curves $P = A(T, I, c_0)R_L/[B(T, I, c_0) + R_L]^2$ demonstrates the distinct roles of parameters A and B, which depend on temperature, electrolyte concentration, and solar intensity. By fitting this expression to the experimental data in **Figure 5B-D**, we have compiled the values of the A and B parameters for a range of different conditions, as shown in **Figure S13**. The peak power output, represented by $P = A/4B$, occurs at a specific load resistance $R_L = B$, indicating that careful tuning of these parameters is crucial. Notably, achieving double the maximum power output at 100 mM compared to 1 mM KCl concentration—despite a lower open circuit voltage—highlights the significant impact of internal resistance on peak power output, as indicated by parameter B in our study model. In fact, the increase in the open circuit voltage with temperature reinforces the need to consider material choices carefully; a transition from TiO₂ to Al₂O₃ yielded remarkable enhancements of 90% and 57% in V_{OC} at 25°C and 70°C, respectively. Corresponding improvements in power output further validate this approach, with increases of 3.6 times at low temperatures and 2.4 times at high temperatures (**Figure 5E**). We estimated that the transfer capacitance for the Al₂O₃ sample is almost 1.8 times higher than the TiO₂ one at 1 mM concentration and 25°C (see **Figure 4C**). Lastly, the influence of silicon doping illustrates another pathway for enhancing power output (**Figure 5F**). High N-doped Al₂O₃ samples displayed a 28% increase in open circuit voltage over low N-doped counterparts, leading to a 1.6-fold improvement in power output. This finding lays the groundwork for future research focused on material engineering to optimize device performance under various environmental conditions. In summary, the interplay between concentration and material properties presents a rich avenue for improving power output in EDHV devices operating under the influence of external heating and solar illumination.

The experimental results consistent with the proposed model demonstrate significant enhancements in power output due to the influence of heat and light. This improvement is not solely a result of increased evaporation but also of the improved ion dynamics caused by light-induced photocharging at the silicon-oxide interface and the thermally enhanced chemical

potential at the oxide-electrolyte interface. Thus, it provides a unified perspective that incorporates thermodiffusion and photovoltaic effects, in addition to the electrical potential generated at the top evaporating surface.

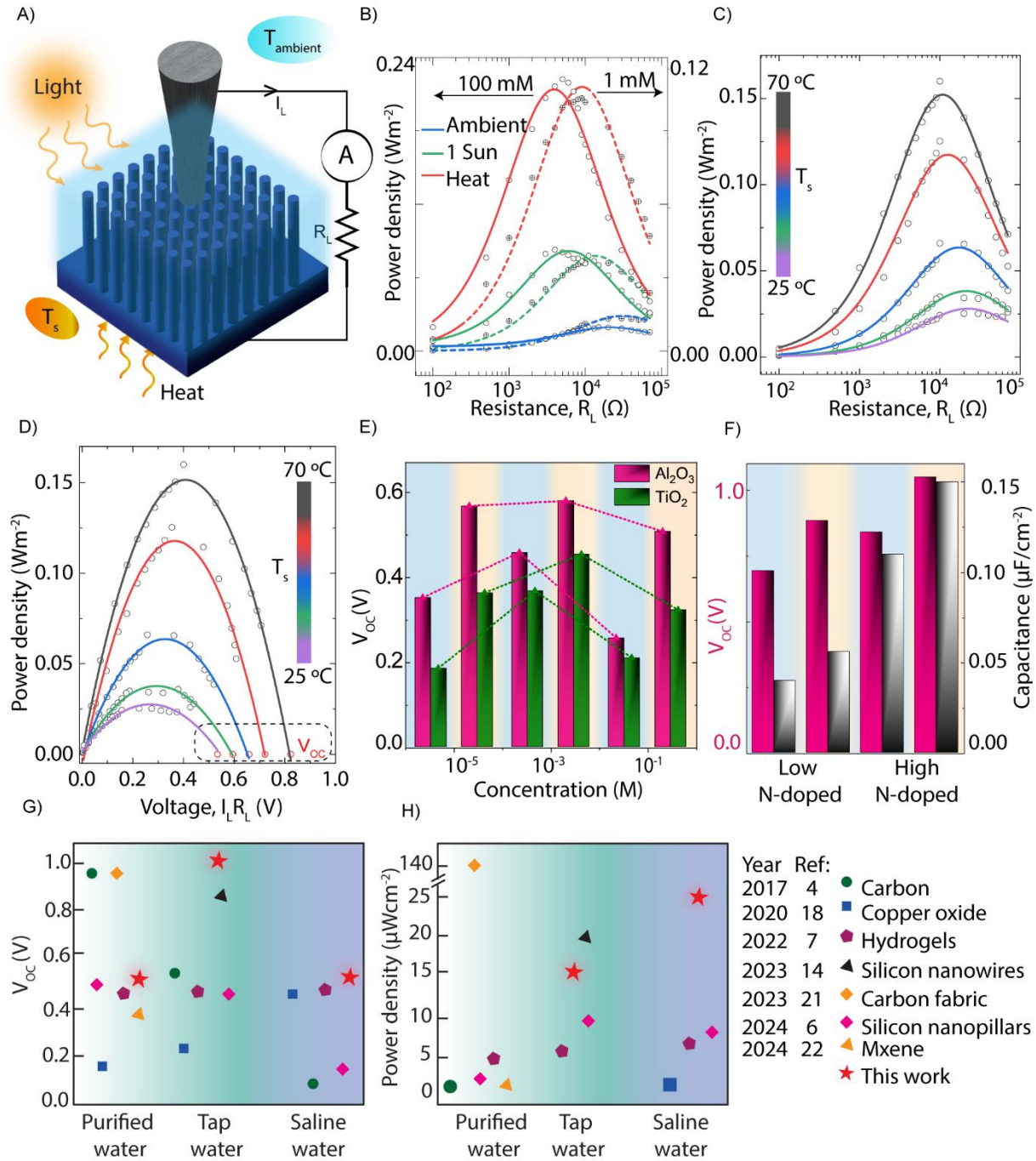


Figure 5: Device Performance as a Function of Materials, Electrolyte, and Environmental Conditions (Heat/Light). A) Schematic representation of the device measurement configuration with various external loads for different surface temperatures and under illumination. The measurements were conducted at ambient temperature with or without

solar illumination or elevated surface temperature. B) Power-load resistance profiles for various conditions (ambient: $T_s = 25^\circ\text{C}$; 1 Sun: 1 kW/m^2 solar intensity and $T_s = 25^\circ\text{C}$; heat: $T_s = 70^\circ\text{C}$) at 1 mM and 100 mM KCl. The profiles demonstrate an increase in peak height and a shift of the peak toward lower resistances under illumination and at elevated temperatures. The empty (crossed) circles represent experimental values, while the solid (dashed) lines illustrate fits based on our model for 1 mM (100 mM) KCl; C) Power-load resistance profiles for various surface temperatures (T_s) at 1 mM KCl demonstrate an increase in peak height and a shift in the peak toward lower resistance at elevated temperatures. The empty circles represent experimental values, while the solid lines depict the fit based on our model. D) The power-voltage profile for different surface temperatures (T_s) at 1 mM KCl demonstrates an increase in peak height at higher temperatures. The rightward shift of the peak indicates that a higher open circuit voltage is achieved at elevated temperatures, as illustrated in the box and red empty circles. The empty circles represent experimental values, while the solid lines represent the fit based on our model; E) Steady-state open circuit voltage values for two devices with Al_2O_3 and TiO_2 dielectric shell but with the same silicon core (Low N-doped: $1\text{-}20\ \Omega\cdot\text{cm}$) at different salinity values. The blue and orange shaded region is measured at a surface temperature of $T_s = T_{\text{ambient}} = 25^\circ\text{C}$ and $T_s = T_H = 70^\circ\text{C}$, respectively. F) Steady-state open circuit voltage and capacitance values for two devices with Al_2O_3 shell, but with the different doping of silicon core (low N-doped: $1\text{-}20\ \Omega\cdot\text{cm}$ and high N-doped: $<0.005\ \Omega\cdot\text{cm}$) at 1 mM KCl. The blue and orange shaded region is measured at a surface temperature of $T_s = T_{\text{ambient}} = 25^\circ\text{C}$ and $T_s = T_H = 70^\circ\text{C}$, respectively. G) Open circuit voltage and H) power density comparison at different levels of salt concentrations for various EDHV devices.

Conclusion

In summary, this study presents a novel unified framework for evaporation-driven hydrovoltaic devices, significantly enhancing their efficacy by incorporating thermodiffusion and photovoltaic effects, transcending the electrical potential generated solely due to ion streaming at the evaporating surface. By using a combination of experiments, numerical calculations, and theoretical modeling, we reveal a mechanism where thermally and light-assisted ion migration, along with the movement of electrolyte near the 3-phase contact boundary, plays a crucial role in energy conversion, achieving a notable open-circuit voltage of up to 1V and an output power density of 0.25W/m^2 at high salt concentrations (0.1M), extending the applicability of hydrovoltaic devices to more practical scenarios. Interestingly, we can decouple the upper evaporating surface from the lower nanostructure through the intermediate electrolyte layer, allowing for increased flexibility in creating optimal structure designs. This approach preserves a chemical potential difference and promotes ion migration, which can be quantified by the transfer capacitance in the suggested equivalent electrical circuit. The experimental results consistent with the proposed model demonstrate significant enhancements in power output due to the influence of heat and light. Importantly, this improvement is not solely a result of increased evaporation but also from the improved ion dynamics caused by light-induced photocharging at the silicon-oxide interface and the thermally enhanced chemical potential at the oxide-electrolyte interface. The material selection, notably the transition from TiO_2 to Al_2O_3 and increased silicon doping, dramatically

influences device performance, suggesting pathways for further optimization. This research lays the groundwork for future studies focusing on material engineering and operational strategies considering environmental factors, ultimately advancing the efficiency and efficacy of renewable energy utilization through EDHV devices. Thus, it provides a unified perspective that incorporates thermodiffusion and photovoltaic effects, in addition to the electrical potential generated at the top evaporating surface.

Methods

Fabrication of core-shell Silicon nanopillars array

Metal-assisted chemical etching (MACE) of crystalline silicon combined with nanosphere lithography was used to fabricate a cm-scale array of SiNPs³⁷. It involves the self-assembly of polystyrene nanospheres at the water-air interface. Then, the non-closed-packed assembly of PS nanospheres was compressed to a pressure of approximately 25-30(N/m²) using the Langmuir-Blodgett system, which resulted in a homogeneous closed-packed hexagonal lattice of PS nanospheres³⁸. The closed-packed monolayer was transferred to Piranha-cleaned Silicon (P-type 0.1-0.5 Ω.cm, and N-type <0.005 and 1-20 Ω.cm) substrates diced into 2cm X 2cm chips. Plasma etching was used to reduce the diameter of the PS nanospheres with an initial diameter of $d = 400\text{nm}$. After the gold-sputtering deposition of a thickness of 20nm and lift-off, a gold nanomesh is formed and used as an etching mask for MACE. Before gold sputtering, 2-3 nm of Ti is sputtered as an adhesion layer. This forms a stable contact between gold and the substrate to avoid delamination during MACE. The liftoff was done by putting the substrate in Toluene and ultrasonicing it at moderate power for 3-5 minutes at room temperature. Finally, MACE was performed by placing the substrate in an aqueous HF/H₂O₂ solution with a volumetric percentage of HF and H₂O₂ as 10% and 2%, respectively. The diameter of the NPs is controlled by changing the time of plasma trimming of the polystyrene nanosphere, while the length of the NPs is controlled by changing the MACE time. The fabricated SiNPs were then surrounded by a shell of dielectric material such as Al₂O₃ and TiO₂ using atomic layer deposition, using trimethylaluminum (TMAI) and titanium tetrachloride (TiCl₄) as aluminum and titanium precursors, respectively. The

obtained sample was then treated with oxygen plasma (60 sec, 1000 W) to improve the hydrophilicity.

Electrical & Thermal Measurements

Figures 1A, 5A, and S2 illustrate the configuration for electrical measurements, where SiNPs serves as the active substrate, and the Al layer functions as the back electrode, while Ag/AgCl (unless stated otherwise) is employed as the top electrode. We used an Ag/AgCl electrode as it is considered fully reversible, which ensures that the electrodes entirely consume the charges accumulated in its EDL at overpotentials, which are practically zero. There is no unwanted potential difference, which induces a conduction current. The open circuit voltage and complex impedance measurements were done using CHI bipotentiostat. The impedance measurements were done at zero applied DC voltage with an amplitude of 5mV at a field frequency of 1 kHz. The resistance was added to the circuit to measure voltage and power at different load resistances. The bipotentiostat was connected in series or parallel for current or voltage measurements, respectively. For temperature-dependent measurements: by changing the voltage applied to the Peltier element, the device's temperature varied from an ambient temperature of 25 °C to 70°C. Temperature is measured using an Infrared camera (Fortric 600s) with 0.2 frames per second. A type-K thermocouple was used for calibration (**Figure S14**). A solar simulator (Newport 66 984-300XF-R1 Xe lamp) with an AM 1.5 G filter was used as the light source for the light dependent study. The electrical measurements were performed similarly to the ambient conditions described above. After each measurement, the samples were carefully rinsed with Isopropanol, followed by DI water. Then the sample was put in a DI water bath (maintained at 60°C) for 5-10 mins with continuous stirring at 500 RPM. Then, finally, the sample was put in the oven maintained at 80°C. Furthermore, to minimize the effect of salt precipitation on the output, the sweep of concentration was always performed starting from DI water followed by low concentration and then higher concentrations. Therefore, for the present study, we expect the effect of salt precipitation at high concentrations to be minimal. We have verified the measurement repeatability at 2 M and 4 M KCl concentrations (**Figure S15**).

Deriving analytical expression for the performance metrics

The streaming of ions in the meniscus region is due to evaporation-induced fluid flow, given by the total space charge density available times the evaporating velocity. The total space charge density is the sum of self-charge density $\bar{\sigma}$ (when the electrode was inserted in a bulk electrolyte) and the charge density arising due to chemical potential difference (Φ).

$$I_{Evap} = W v_f (\bar{\sigma} + C_{tr} \Phi) \quad (M1)$$

The current driven through the load resistance is obtained by solving the equivalent electrical circuit. The resistive element $R_{3\Phi} = \rho_{3\Phi} \frac{L}{W} = \frac{r_{3\Phi}}{W}$, where L and W are the length and perimeter of the meniscus region. So, we use $r_{3\Phi}$ instead, as it is independent of top electrode size.

$$I_L = \frac{I_{\Delta T} R_{Sol} (1 + v_f r_{3\Phi} C_{tr}) + v_f \bar{\sigma} r_{3\Phi} + V_{ph}}{R_{Si} + R_{Sol} (1 + v_f r_{3\Phi} C_{tr}) + r_{3\Phi} / W + R_C + R_L} \quad (M2)$$

The Open Circuit voltage is obtained according to the conditions, $I_L R_L (R_L \rightarrow \infty)$, and under no current through the external load, we have the relation satisfying $I_{\Delta T} R_{Sol} = \Phi$. Thus,

$$V_{OC} = \Phi (1 + v_f r_{3\Phi} C_{tr}) + v_f \bar{\sigma} r_{3\Phi} + V_{ph} \quad (M3)$$

Using Ohm's law, we obtained the power consumed by the resistive load, and it is given by:

$$P(R_L) = \frac{[I_{\Delta T} R_{Sol} (1 + v_f r_{3\Phi} C_{tr}) + v_f \bar{\sigma} r_{3\Phi} + V_{ph}]^2 R_L}{[R_{Si} + R_{Sol} (1 + v_f r_{3\Phi} C_{tr}) + r_{3\Phi} / W + R_C + R_L]^2} = \frac{A(T, I, c_0) R_L}{[B(T, I, c_0) + R_L]^2} \quad (M4)$$

By incorporating the condition of maximum power, $\frac{d(I_L^2 R_L)}{dR_L} = 0$, we obtained the value of load resistance and voltage in terms of the functions A and B, as follows:

$$R_L = B(T, I, c_0) \quad (M5) \quad V = \frac{\sqrt{A(T, I, c_0)}}{2} \quad (M6) \quad P_{max} = \frac{A(T, I, c_0)}{4B(T, I, c_0)} \quad (M7)$$

Numerical calculation to obtain the voltage-temperature dependence

We developed a 3D numerical model (COMSOL®) to solve the Nernst-Planck-Poisson equation to determine the equilibrium distribution of ions and resulting electrostatic potentials. To perform these calculations, however, we must first identify an equivalent simplified geometry using the

approach described in our prior work⁶. The simulation details, such as package use and boundary conditions, are given in **Figure S16**. The following equilibrium reactions govern the amount of surface charge in an oxide-aqueous interface. $MOH + H_2O \Leftrightarrow MO^- + H_3O^+$. The equilibrium constant for this reaction is given by $K_a = [H_3O^+][MiO^-]/[MOH][H_2O]$, which is temperature-dependent³⁹. The temperature dependence is governed by:

$$K_a = K_{a0} \exp \left[-\frac{\Delta_H}{R} \left(\frac{1}{T} - \frac{1}{T_0} \right) \right] \quad (M8)$$

where the material's chemical characteristic, Δ_H , is the enthalpy of dissociation of the surface groups. We used surface charge density as the boundary condition, which is not a fixed value but is instead governed by the above equilibrium reaction. This results in variable surface charge density that depends on the surface potential at the stern plane⁴⁰, given by the following equation:

$$\Psi_0(\sigma) = \frac{k_B T}{e} \left[\ln \left(\frac{-\sigma}{\sigma + e\Gamma} \right) - \ln(10)(pH - pK) \right] \quad (M9)$$

This enabled us to obtain the open circuit voltage as a function temperature for various conditions, such as by varying electrolyte concentration, pH, and K_{a0} . Then, we swept Δ_H , and obtained voltage-temperature lines for various conditions. Finally, we constructed the correlation between the slopes of Voltage-temperature lines and the value of Δ_H .

Acknowledgment: T.A. and G.T. acknowledge the support of the Swiss National Science Foundation (Starting Grant 211695 and Korean-Swiss Science and Technology Cooperation Fund IZKSZ2_188341). T.A. also acknowledges the support of Swiss Government Excellence fellowship. The authors acknowledge the support of Milad Sabzehparvar for his assistance in Scanning Electron Microscopy imaging and Vasily Artemov for helpful discussions during the manuscript preparation. The authors also acknowledge the support of the following experimental facilities at EPFL: Center of MicroNanoTechnology (CMi) and Interdisciplinary Centre for Electron Microscopy (CIME).

Author contributions: G.T. and T.A. conceived the study. T.A. conducted the experiments and developed the models under the supervision of G.T. All authors contributed to writing and revising the manuscript.

Declaration of interests

The authors declare no competing interests.

References

1. Cavusoglu, A.-H., Chen, X., Gentine, P. & Sahin, O. Potential for natural evaporation as a reliable renewable energy resource. *Nat Commun* **8**, 617 (2017).
2. Fang, S., Li, J., Xu, Y., Shen, C. & Guo, W. Evaporating potential. *Joule* **6**, 690–701 (2022).
3. Song, D. *et al.* Conveyor mode enabling continuous ionic thermoelectric conversion. *Joule* **8**, 3217–3232 (2024).
4. Xue, G. *et al.* Water-evaporation-induced electricity with nanostructured carbon materials. *Nature Nanotech* **12**, 317–321 (2017).
5. Zhang, Z. *et al.* Emerging hydrovoltaic technology. *Nature Nanotech* **13**, 1109–1119 (2018).
6. Anwar, T. & Tagliabue, G. Salinity-dependent interfacial phenomena toward hydrovoltaic device optimization. *Device* **2**, 100287 (2024).
7. Sun, Z. *et al.* Achieving efficient power generation by designing bioinspired and multi-layered interfacial evaporator. *Nat Commun* **13**, 5077 (2022).
8. Shao, B. *et al.* Boosting electrical output of nanostructured silicon hydrovoltaic device via cobalt oxide enabled electrode surface contact. *Nano Energy* **106**, 108081 (2023).
9. Mandal, S. *et al.* Protein-Based Flexible Moisture-Induced Energy-Harvesting Devices As Self-Biased Electronic Sensors. *ACS Appl. Electron. Mater.* **2**, 780–789 (2020).
10. Cheng, H. *et al.* Flexible in-plane graphene oxide moisture-electric converter for touchless interactive panel. *Nano Energy* **45**, 37–43 (2018).
11. Shen, D. *et al.* Self-Powered, Rapid-Response, and Highly Flexible Humidity Sensors Based on Moisture-Dependent Voltage Generation. *ACS Appl. Mater. Interfaces* **11**, 14249–14255 (2019).
12. Brückner, S. *et al.* Industrial waste heat recovery technologies: An economic analysis of heat transformation technologies. *Applied Energy* **151**, 157–167 (2015).
13. Papapetrou, M., Kosmadakis, G., Cipollina, A., La Commare, U. & Micale, G. Industrial waste heat: Estimation of the technically available resource in the EU per industrial sector, temperature level and country. *Applied Thermal Engineering* **138**, 207–216 (2018).
14. Li, L. *et al.* Enhancing hydrovoltaic power generation through heat conduction effects. *Nat Commun* **13**, 1043 (2022).
15. Yoon, S. G. *et al.* Natural Evaporation-Driven Ionovoltaic Electricity Generation. *ACS Appl. Electron. Mater.* **1**, 1746–1751 (2019).
16. Wang, L., Liu, L. & Solin, N. Ionovoltaic electricity generation over graphene-nanoplatelets: protein-nanofibril hybrid materials. *Nanoscale Adv.* **5**, 820–829 (2023).

17. Qin, Y. *et al.* Constant Electricity Generation in Nanostructured Silicon by Evaporation-Driven Water Flow. *Angewandte Chemie International Edition* **59**, 10619–10625 (2020).
18. Jin, H. *et al.* Identification of water-infiltration-induced electrical energy generation by ionovoltaic effect in porous CuO nanowire films. *Energy & Environmental Science* **13**, 3432–3438 (2020).
19. Shuvra Das, S., Kar, S., Anwar, T., Saha, P. & Chakraborty, S. Hydroelectric power plant on a paper strip. *Lab on a Chip* **18**, 1560–1568 (2018).
20. Yaroshchuk, A. Evaporation-driven electrokinetic energy conversion: Critical review, parametric analysis and perspectives. *Advances in Colloid and Interface Science* **305**, 102708 (2022).
21. Yu, F. *et al.* High Hydrovoltaic Power Density Achieved by Universal Evaporating Potential Devices. *Advanced Science* **10**, 2302941 (2023).
22. Xia, H. *et al.* Electricity generated by upstream proton diffusion in two-dimensional nanochannels. *Nat. Nanotechnol.* 1–7 (2024) doi:10.1038/s41565-024-01691-5.
23. Gao, M., Zhu, L., Kangnuo Peh, C. & Wei Ho, G. Solar absorber material and system designs for photothermal water vaporization towards clean water and energy production. *Energy & Environmental Science* **12**, 841–864 (2019).
24. Fu, L., Joly, L. & Merabia, S. Giant Thermoelectric Response of Nanofluidic Systems Driven by Water Excess Enthalpy. *Phys. Rev. Lett.* **123**, 138001 (2019).
25. Ouadfel, M., Féliciano, M. D. S., Herrero, C., Merabia, S. & Joly, L. Complex coupling between surface charge and thermo-osmotic phenomena. *Physical Chemistry Chemical Physics* **25**, 24321–24331 (2023).
26. Gonella, G. *et al.* Water at charged interfaces. *Nat Rev Chem* **5**, 466–485 (2021).
27. Artemov, V. *et al.* The Three-Phase Contact Potential Difference Modulates the Water Surface Charge. *J. Phys. Chem. Lett.* **14**, 4796–4802 (2023).
28. Sun, M., Lu, Q., Wang, Z. L. & Huang, B. Understanding contact electrification at liquid–solid interfaces from surface electronic structure. *Nat Commun* **12**, 1752 (2021).
29. Lin, S., Xu, L., Chi Wang, A. & Wang, Z. L. Quantifying electron-transfer in liquid-solid contact electrification and the formation of electric double-layer. *Nat Commun* **11**, 399 (2020).
30. Sposito, G. On the surface complexation model of the oxide-aqueous solution interface. *Journal of Colloid and Interface Science* **91**, 329–340 (1983).
31. Li, J. *et al.* Kinetic photovoltage along semiconductor-water interfaces. *Nat Commun* **12**, 4998 (2021).
32. Li, J. *et al.* Passive Gate-Tunable Kinetic Photovoltage along Semiconductor-Water Interfaces. *Angewandte Chemie International Edition* **62**, e202218393 (2023).

33. Richter, A., Patel, H., Reichel, C., Benick, J. & Glunz, S. W. Improved Silicon Surface Passivation by ALD Al₂O₃/SiO₂ Multilayers with In-Situ Plasma Treatments. *Advanced Materials Interfaces* **10**, 2202469 (2023).
34. Bahruji, H., Bowker, M. & Davies, P. R. Photoactivated reaction of water with silicon nanoparticles. *International Journal of Hydrogen Energy* **34**, 8504–8510 (2009).
35. Mizsei, J. Fermi-level pinning and passivation on the oxide-covered and bare silicon surfaces and interfaces. *Vacuum* **67**, 59–67 (2002).
36. Mayer, M. T. Photovoltage at semiconductor–electrolyte junctions. *Current Opinion in Electrochemistry* **2**, 104–110 (2017).
37. Wendisch, F. J., Rey, M., Vogel, N. & Bourret, G. R. Large-Scale Synthesis of Highly Uniform Silicon Nanowire Arrays Using Metal-Assisted Chemical Etching. *Chem. Mater.* **32**, 9425–9434 (2020).
38. Thangamuthu, M., Santschi, C. & Martin, O. J. F. Reliable Langmuir Blodgett colloidal masks for large area nanostructure realization. *Thin Solid Films* **709**, 138195 (2020).
39. Vordonis, L. & Lycourghiotis, A. Effect of Temperature on the Point of Zero Charge and Surface Dissociation Constants of Aqueous Suspensions of γ -Al₂O₃.
40. Behrens, S. H. & Grier, D. G. The charge of glass and silica surfaces. *The Journal of Chemical Physics* **115**, 6716–6721 (2001).

A Unified Framework for Harnessing Heat and Light with Hydrovoltaic Devices: Supplementary Information

Tarique Anwar¹ and Giulia Tagliabue^{1*}

¹Laboratory of Nanoscience for Energy Technologies (LNET), STI, École Polytechnique Fédérale de Lausanne (EPFL), Lausanne 1015, Switzerland

*To whom correspondence should be addressed: E-mail: giulia.tagliabue@epfl.ch

S1: evaporation rate measured with different electrode size

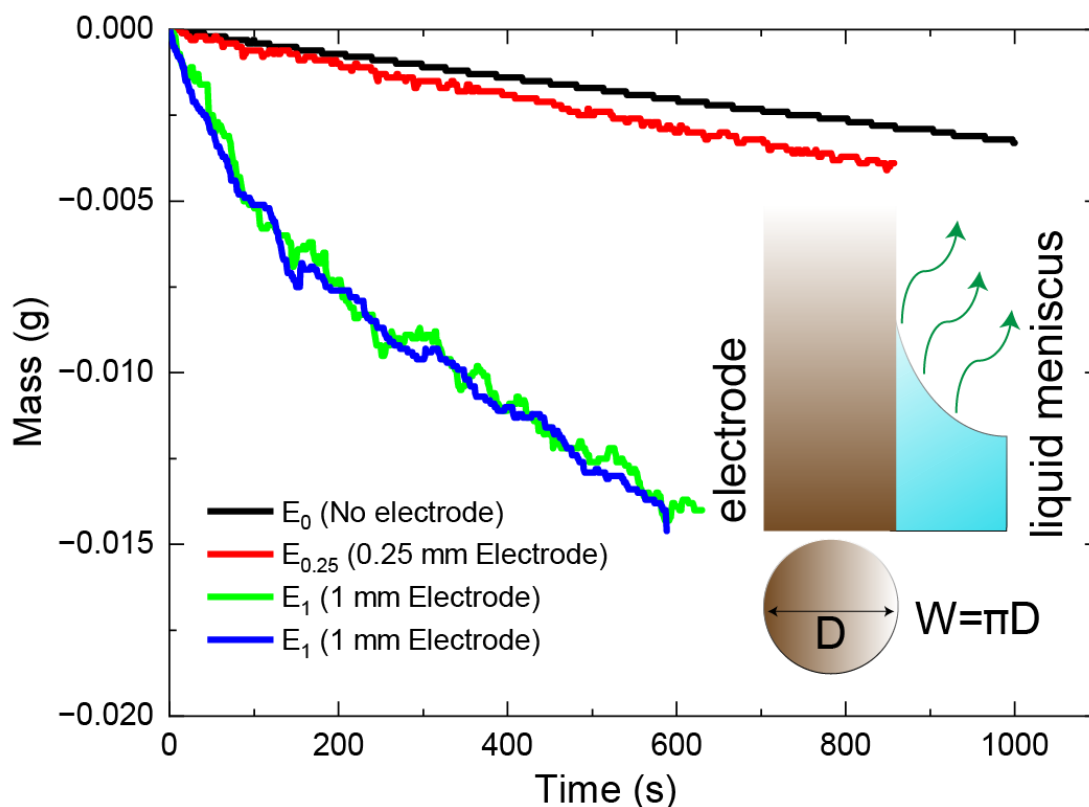
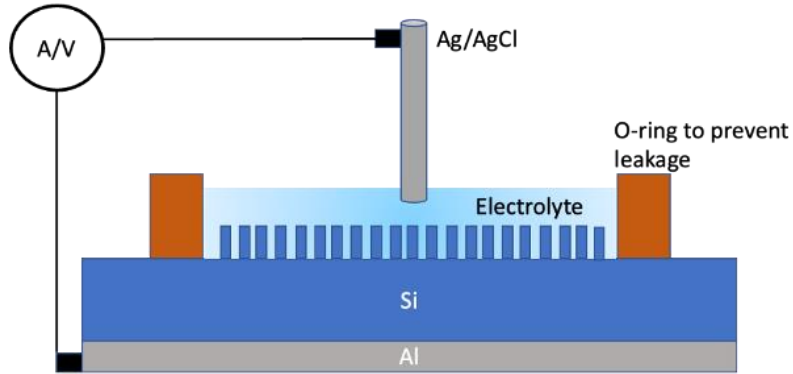


Figure S1: Measured evaporative flux of water in different conditions. The change in mass due to evaporation in an ambient environment was recorded using a microbalance. The Hydrovoltaic cell was placed in the microbalance, then the mass change was monitored in different conditions. i) No electrode was placed in the cell (black curve), ii) 0.25 mm diameter ($W=0.8$ mm) electrode (red curve), iii) 1 mm diameter ($W=3.2$ mm) electrode (blue and green curves).

S2: Hydrovoltaic cell

A)



B)

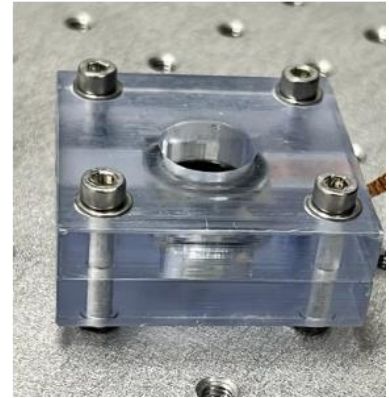


Figure S2: A) Schematic of the cross-sectional view of the measurement set-up. B) Photo of the hydrovoltaic cell showing an active central area of $\sim 1\text{cm}^2$ that is wetted with electrolyte solution while the remaining device is completely dry. The compression cell is made of VeroClear, a transparent material that simulates PMMA (poly-methyl methacrylate). The O-ring is compressed using four corner screws that prevent fluid leakage outside the central region ($\sim 1\text{cm}^2$ area).

S3: Electrical measurements using graphite-electrode

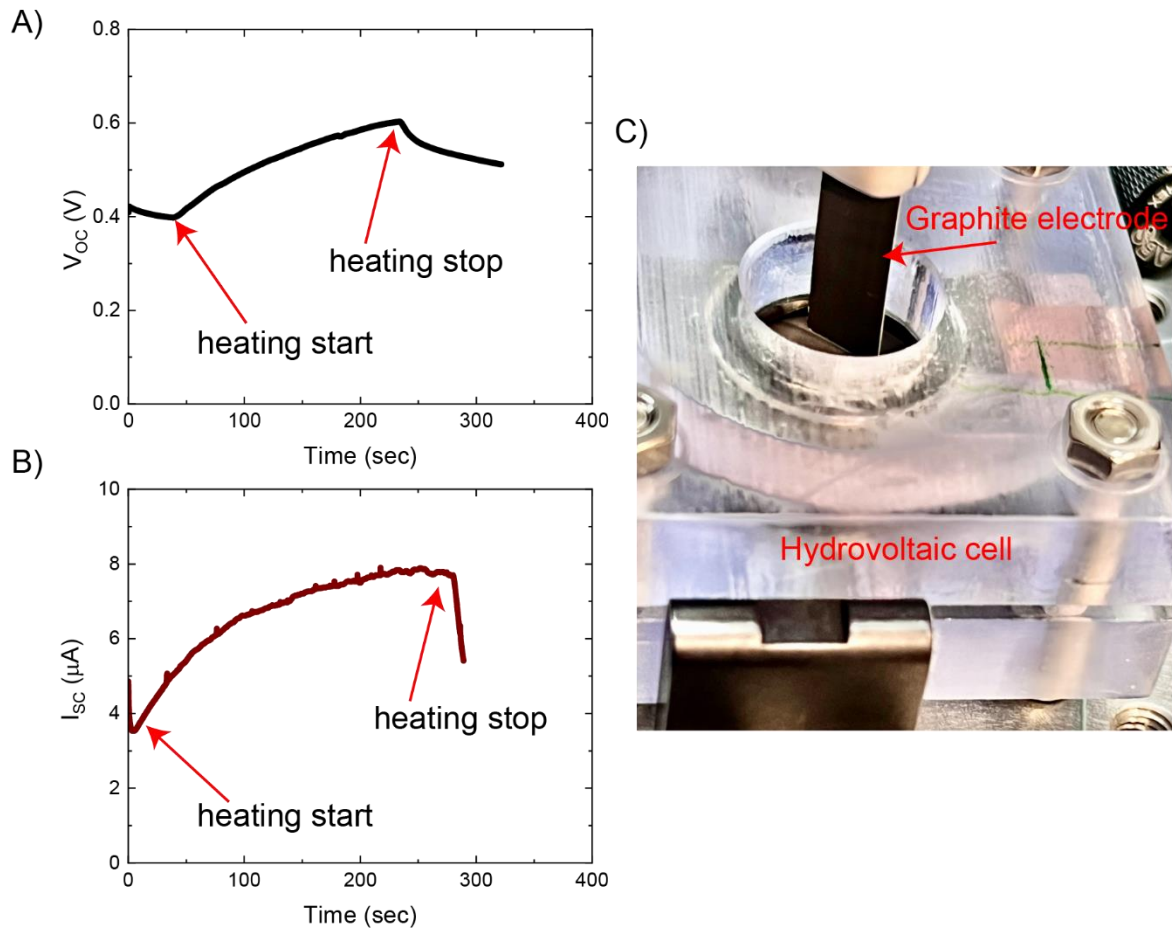


Figure S3: Electrical measurements using graphite electrode at ambient, heating, and cooling phases. **A)** Open circuit voltage, **B)** Short circuit current, **C)** Photo of the Hydrovoltaic cell with the graphite electrode mounted.

S4: Analysis of the temperature measurements

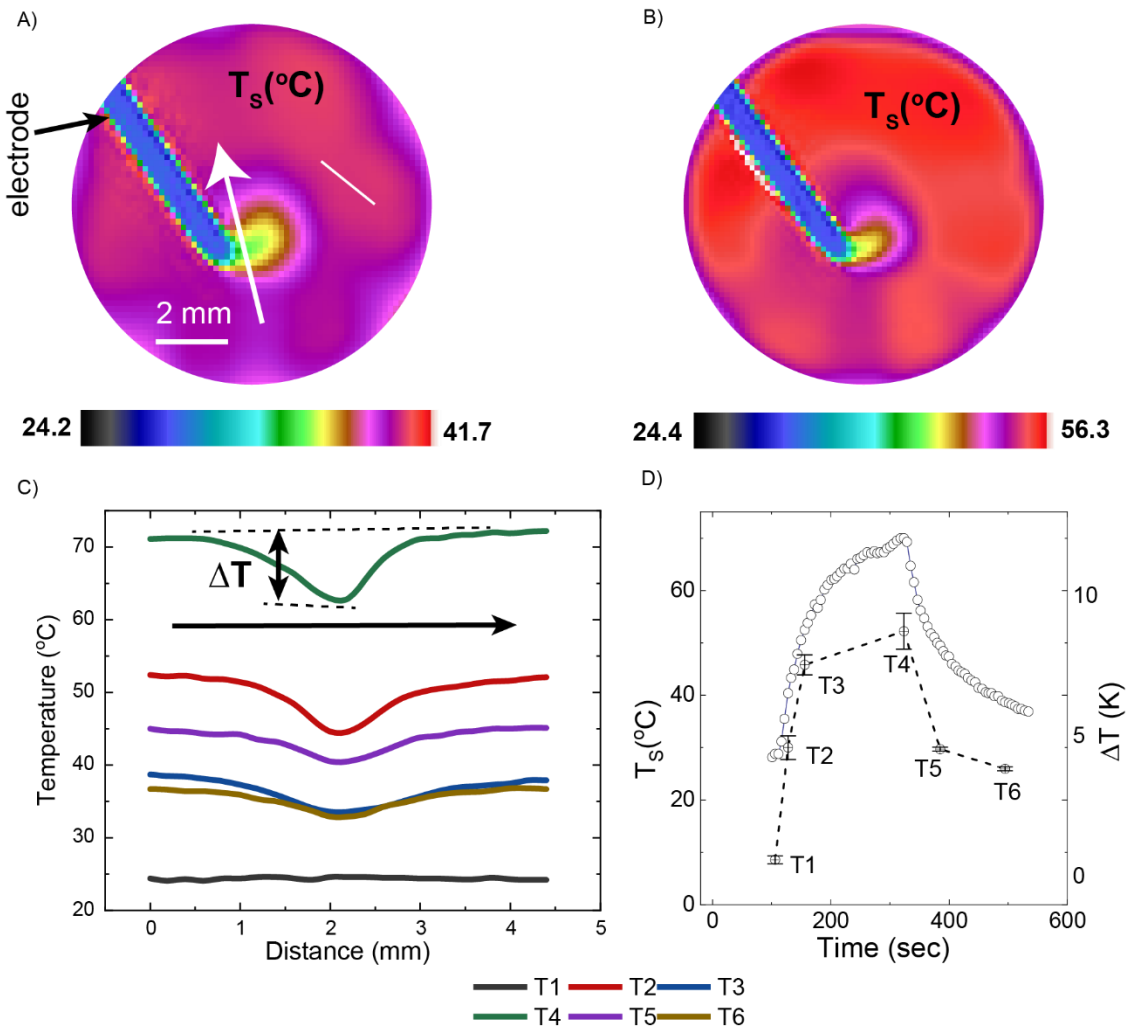


Figure S4: temperature maps obtained using an IR camera. **A)** Temperature map at maximum $T_s=41.7^\circ\text{C}$, **B)** at maximum $T_s=56.3^\circ\text{C}$. **C)** Temperature profile along the indicated white arrow in panel A. **D)** Obtained surface temperature T_s and temperature difference ΔT for the heating and cooling phase.

S5: Open circuit voltage measured for different doping of the silicon core

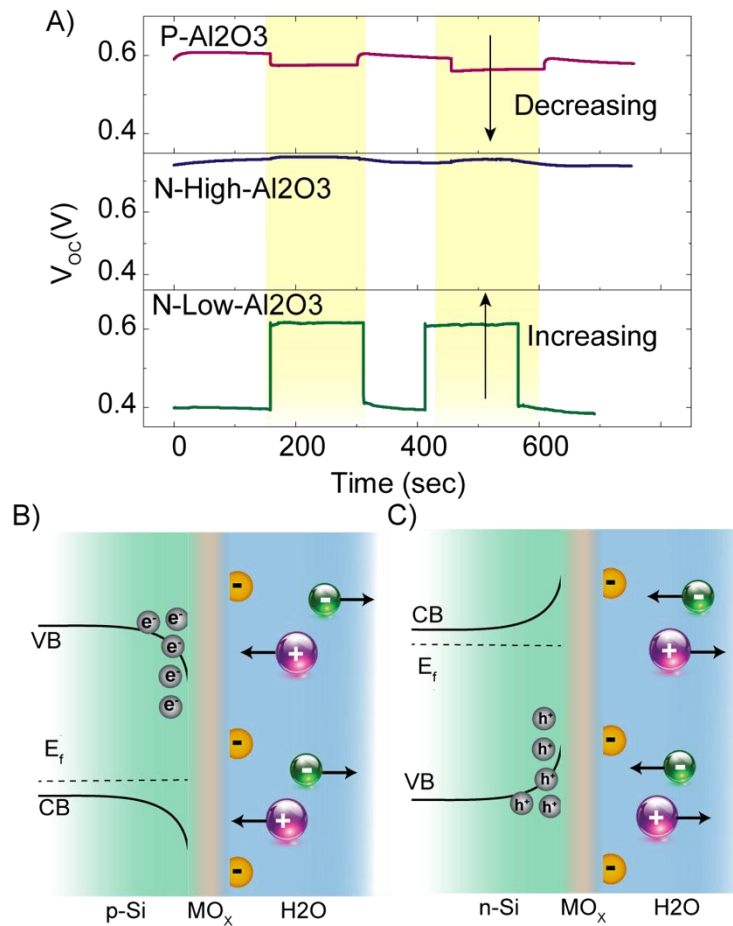


Figure S5: Time trace of the measured open circuit voltage at 1 mM KCl for 3 devices with different doping of the silicon core but with the same Al₂O₃ shell. The test was performed in ambient conditions and under 1 Sun illumination (shaded region). B) Band bending at p-silicon-oxide-electrolyte interface showing accumulation of electrons and movement of cations towards the interface. C) Band bending at n-silicon-oxide-electrolyte interface showing accumulation of holes and movement of cations away from the interface.

S6: Equivalent circuit based on current and voltage sources. Derivation of the transient open circuit voltage.

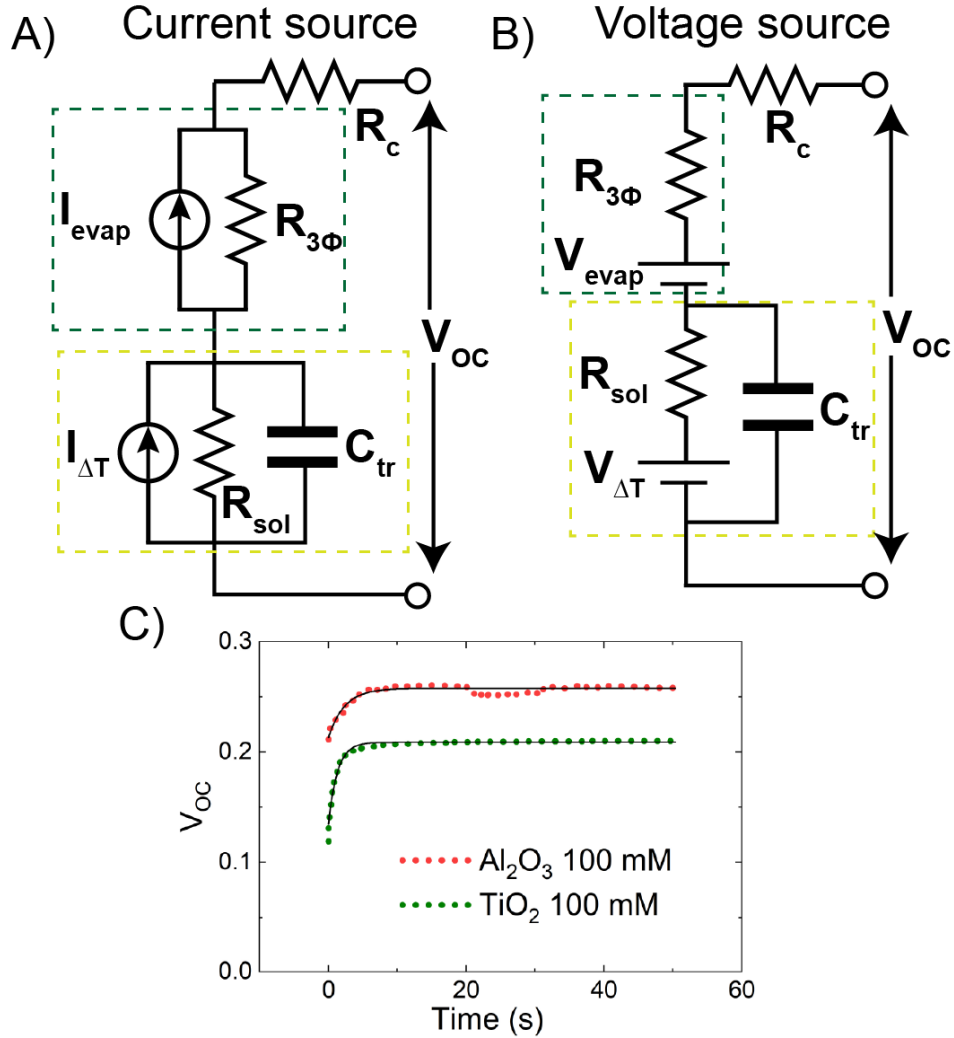


Figure S6: Equivalent electrical circuit for estimating open circuit voltage. A) with a current source. B) with a voltage source. C) Transient voltage curve with the corresponding fit using the derived expression based on a single exponential.

In the transient condition, the charge stored in the capacitor is governed by the following linear differential equation, obtained based on Kirchoff's loop law.

$$\frac{dq_c}{dt} + \frac{q_c}{R_{\text{sol}}C_{\text{tr}}} = \frac{V_{\Delta T}}{R_{\text{sol}}} \quad (\text{S6.1})$$

$$q_c(t) = C_{\text{tr}}V_{\Delta T}e^{-\frac{t}{R_{\text{sol}}R_{\text{ctr}}}}$$

Thus, the open circuit voltage is given by

$$V_{OC}(t) = V_{evap} - V_{\Delta T} \left(1 - e^{-\frac{t}{R_{sol}C_{tr}}} \right) \quad (S6.2)$$

Using the measured open circuit voltage, we obtain the values of the parameter by fitting as follows:

Material (i)	Conc. (j)	V_{evap}^{ij}	$V_{\Delta T}^{ij}$	$(R_{sol}C_{tr})^{ij}$
Al2O3	1 mM	0.358	0.083	1.713
	100 mM	0.260	0.119	2.289
TiO2	1 mM	0.384	0.0076	0.372
	100 mM	0.208	0.0817	1.324

Table S6: Value of the fitting parameters obtained by using single exponential fit.

S7: Open circuit voltage measured with ethanol

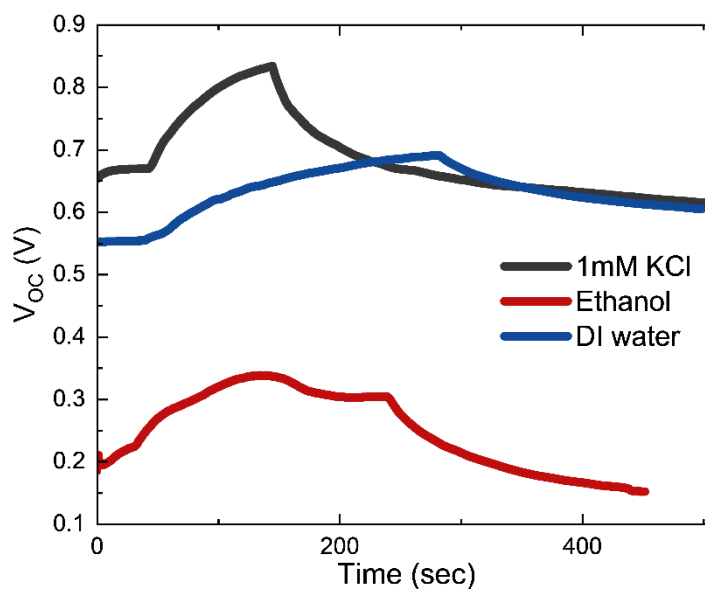


Figure S7: Time trace of the open circuit voltage for a representative sample with different solvents. The time trace shows an initial case of ambient temperature and a heating phase followed by a cooling phase. The voltage is significantly lower for ethanol compared to water. Furthermore, having ions in the solvent (1mM KCl cases) increases the open circuit voltage due to the higher chemical potential difference.

S8: Voltage-temperature lines obtained using COMSOL Multiphysics model

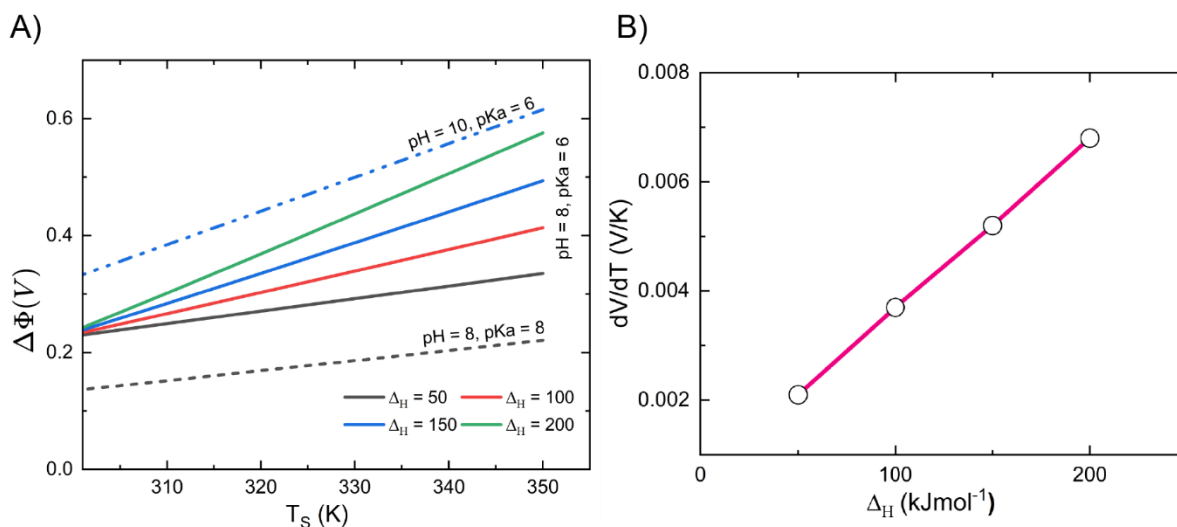


Figure S8: The slope of voltage-temperature lines for various conditions. A) Chemical potential difference as a function of temperature for various conditions of pH, pKa, and Δ_H . The slope of voltage temperature depends mostly on the oxide's surface chemical characteristic, Δ_H , which is the enthalpy of dissociation of the surface groups¹. **B)** The slope dV/dT , plotted as a function of Δ_H , shows a linear dependence.

S9: Fitting of voltage-temperature curves

We used the measured voltage-temperature curves to obtain the equivalent electrical circuit parameters in **S10**. $V_{OC}^{ij}(T)$ can be fitted using a quadratic temperature dependence, where i stands for different materials, and j is for electrolyte concentrations. The parameters are given in the table below.

$$V_{OC}^{ij}(T) = A_{ij}T^2 + B_{ij}T + C_{ij}$$

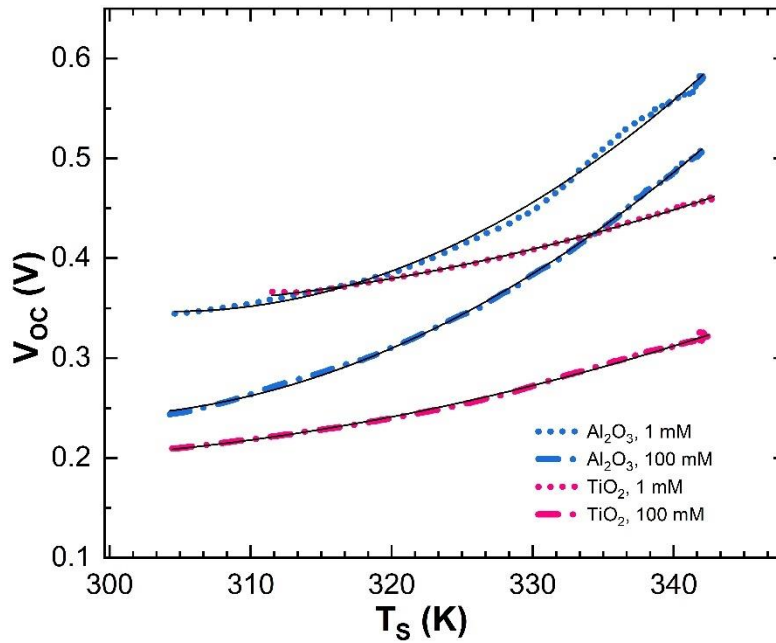


Figure S9: Measured Voc with temperature and the fit with the quadratic line.

Material (i)	Conc. (j)	A_{ij}	B_{ij}	C_{ij}
Al ₂ O ₃	1 mM	1.7e-4	-0.01	0.517
	100 mM	1.4e-4	-0.007	0.331
TiO ₂	1 mM	5.0e-5	-0.0023	0.376
	100 mM	4.0e-5	-0.001	0.2

Table S9: Value of the fitting parameters obtained by using quadratic fit.

S10: Derivation of the expression for $r_{3\phi}$ for 1 mM and 100 mM concentrations

The expression for open circuit voltage as a function of temperature for the two dielectric shell materials Al₂O₃ (i=1), and TiO₂ (i=2), and concentrations of electrolyte 1 mM (j=1), and 100 mM (j=2) is given by:

$$V_{OC}^{ij}(T) = (v_f \bar{\sigma} r_{3\phi})^j + \Phi^{ij} \left(1 + \left(\frac{v_f r_{3\phi}}{R_{sol}} \right)^j (R_{sol} C_{tr})^{ij} \right) \quad (S10.1)$$

It is reasonable to assume, that the variables like $v_f, \bar{\sigma}, r_{3\phi}$ does not change when the materials on the bottom SiNPs electrode changes, as long as the top electrode are the same. This allows us to determine the expression for $v_f r_{3\phi}$ as a function of temperature for different electrolyte concentrations.

The chemical potential difference, Φ , can be expressed as a linear function of temperature as follows, where Φ_0 is at ambient temperature T_0 . The slope, k , is obtained from the linear part of voltage-temperature curves. The value of Φ_0 is approximated as $V_{\Delta T}$ as described in **S6**.

$$\Phi^{ij} = \Phi_0^{ij} + k^{ij}(T_S - T_0) \quad (S10.2)$$

$$k^{ij} = \begin{bmatrix} 0.0041 & 0.0045 \\ 0.0025 & 0.0027 \end{bmatrix} (VK^{-1}) \quad (S10.3)$$

Thus, we obtained the functional dependence of $r_{3\phi}$ with temperature for different concentrations using the measured open circuit voltage and our proposed model.

$$\left(\frac{v_f r_{3\phi}}{R_{sol}} \right)^j = \frac{V_{OC}^{1j}(T) - V_{OC}^{2j}(T) - (\Phi^{1j} - \Phi^{2j})}{(R_{sol} C_{tr} \Phi)^{1j} - (R_{sol} C_{tr} \Phi)^{2j}} \quad (S10.4)$$

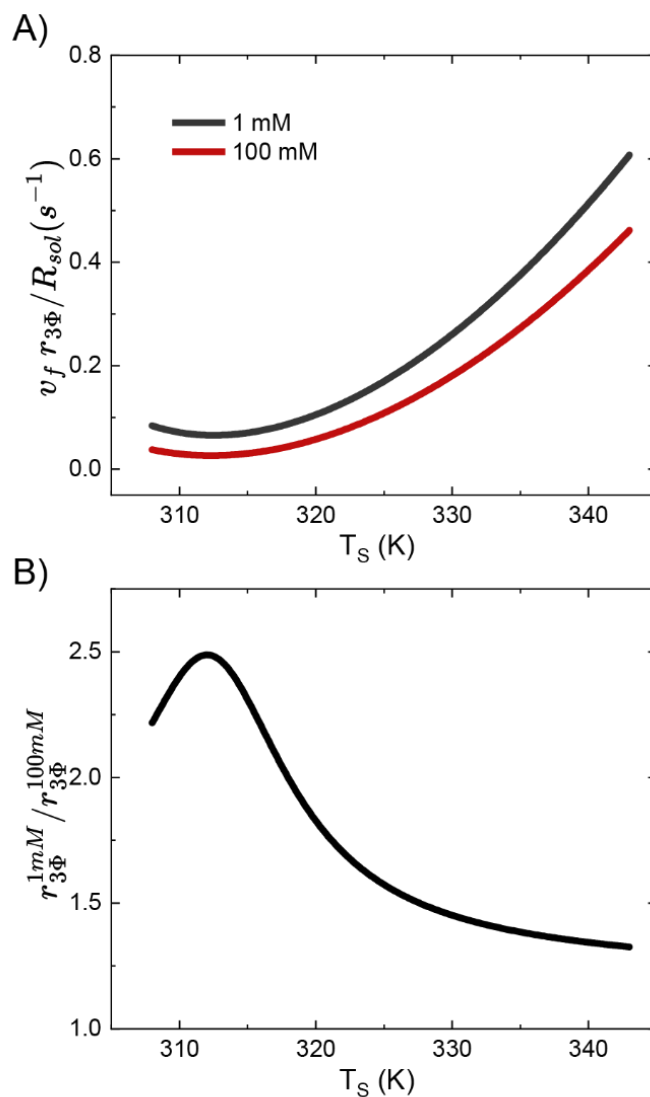


Figure S10: Estimating the functional form of 3-phase resistance. A) Normalized by the solution resistance, which is a function of temperature. B) Ratio of 3-phase resistance as a function of temperature normalised by the ratio of electrolyte conductivities (conductivity of 100 mM KCl / conductivity of 1 mM KCl ≈ 84) at ambient temperature of 25 °C.

S11: Open circuit voltage with and without Al₂O₃

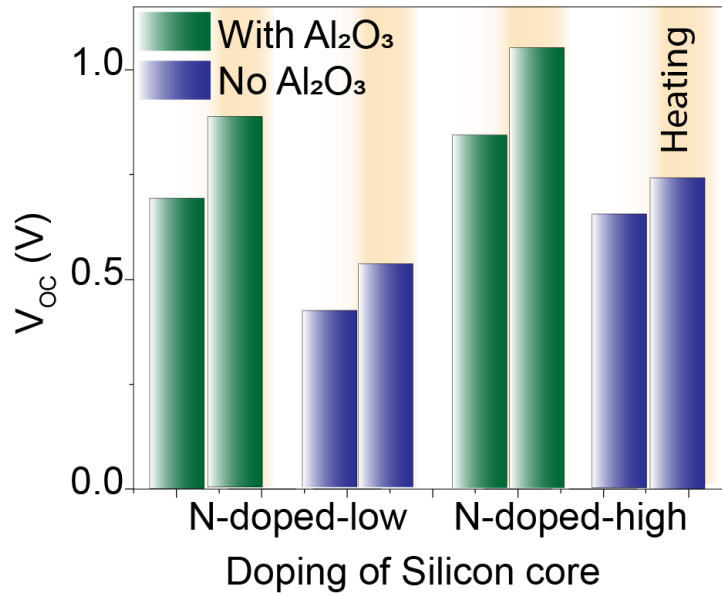


Figure S11: Open circuit voltage for different silicon core, with (green) and without (blue) Al₂O₃. The unshaded regions are for $T_s = 25^\circ\text{C}$, while the shaded regions are for $T_s = 70^\circ\text{C}$. The electrolyte concentration is 1mM. Remarkably, for all the tested conditions, the voltage is higher for samples with Al₂O₃ coating.

S12: Derivation of differential capacitance for the Electrical Double Layer

$$\Phi = \frac{2k_B T_S}{e} \sinh^{-1} \left(\frac{\sigma(T_S)}{\sqrt{8000 \epsilon_0 \epsilon_r c_0 k_B T_S}} \right) + \frac{\sigma(T_S)}{C_{stern}} \quad (S12.1)$$

The differential capacitance is given by:

$$C = \frac{\partial \sigma}{\partial \Phi} \quad (S12.2)$$

$$\frac{1}{C} = \frac{1}{C_d} + \frac{1}{C_{stern}} = \frac{\partial \Phi}{\partial \sigma} \quad (S12.3)$$

$$\frac{\partial \Phi}{\partial \sigma} = \frac{2k_B T_S}{e} \frac{1}{\sqrt{8000 \epsilon_0 \epsilon_r c_0 k_B T_S + \sigma^2}} + \frac{1}{C_{stern}} \quad (S12.4)$$

$$C_d = \frac{e}{2k_B T_S} \sqrt{8000 \epsilon_0 \epsilon_r c_0 k_B T_S + \sigma^2} \quad (S12.5)$$

S13: Obtaining the parameters from the power curves.

$$P(R_L) = \frac{[I_{\Delta T} R_{Sol}(1 + v_f r_{3\phi} C_{tr}) + v_f \bar{\sigma} r_{3\phi} + V_{ph}]^2 R_L}{[R_{Si} + R_{Sol}(1 + v_f r_{3\phi} C_{tr}) + r_{3\phi}/W + R_c + R_L]^2} = \frac{A(T, I, c_0) R_L}{[B(T, I, c_0) + R_L]^2}$$

The values of the parameters A and B obtained are shown below:

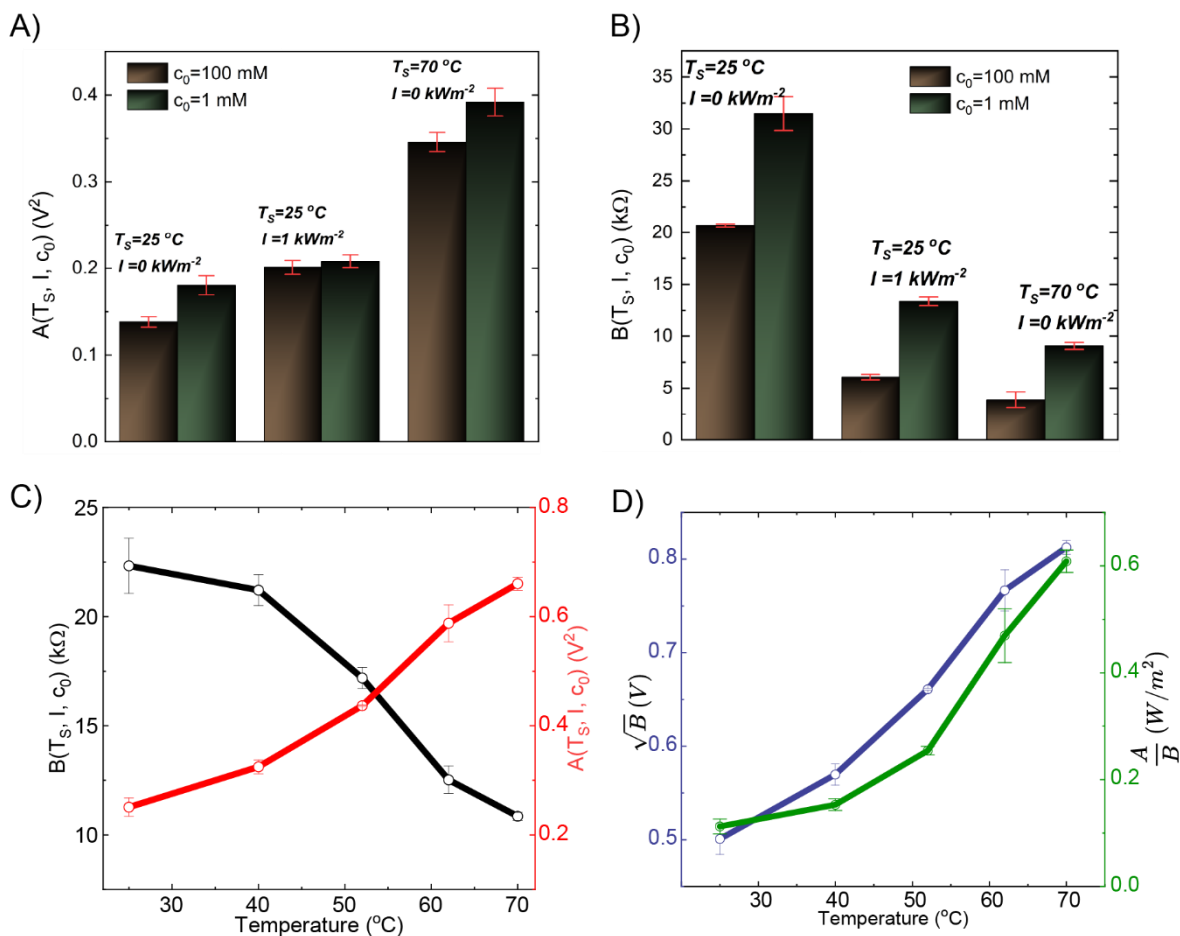


Figure S13: Determining the value of the parameters A and B under different conditions. A) Values of A. B) values of B. C) Values of A (red curve) and B (black curve) at 1 mM concentration as a function of temperature when there is no incident light. D) Values of A and B in a different functional form, which scales as voltage (blue curve) and power (green curves).

S14: calibration using thermocouple

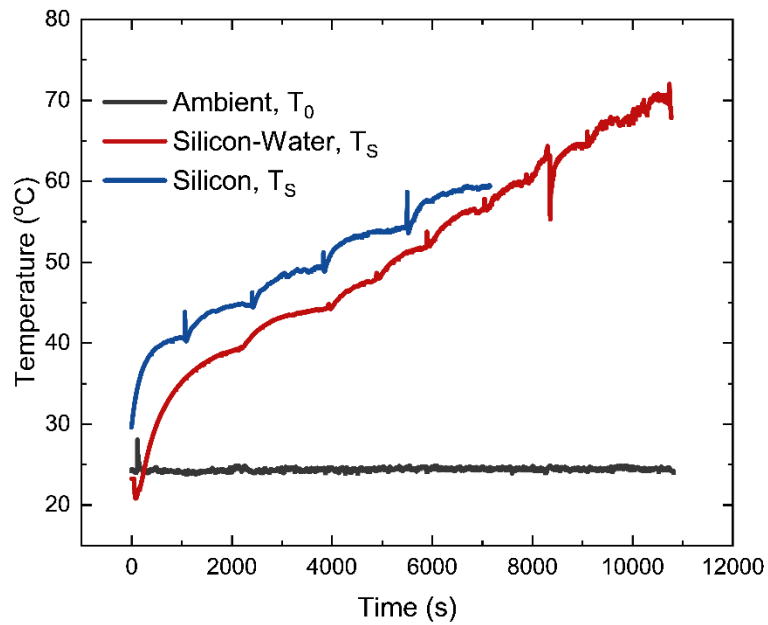


Figure S14: Temperature of silicon substrate measured in the HV cell. The black curve shows the ambient temperature. The red and blue curves show the temperature of the silicon substrate with wetted and un-wetted conditions of the experiments. The temperature is gradually increased by changing the voltage supplied to the heater until a maximum temperature of 70°C is reached. The slight temperature difference between the blue and red lines is due to the higher heat loss pathways in the wetted condition.

S15: Repeatability test at very high concentrations of KCl

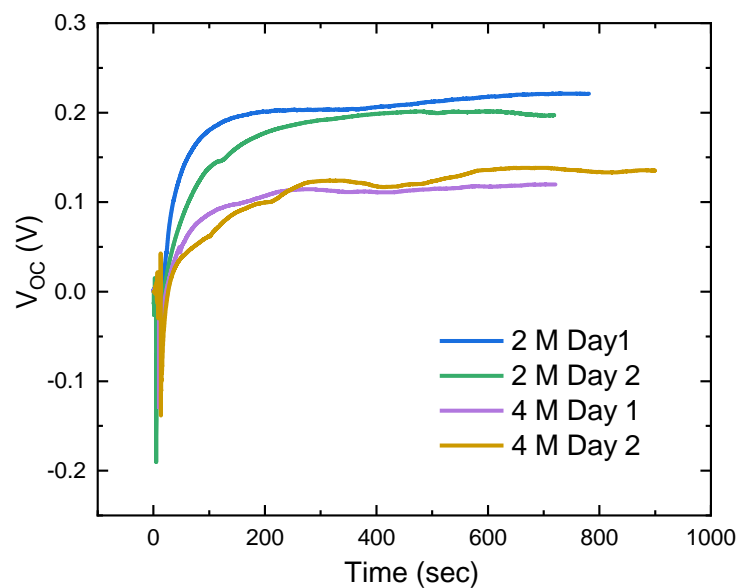


Figure S15: Repeatability test at high concentrations. Time evolution of open circuit voltage from a particular sample at 2M and 4M KCl concentrations performed on two different days.

S16: COMSOL model

We developed a 3D numerical model (COMSOL®) to solve the Nernst-Planck-Poisson equation to determine the equilibrium distribution of ions and resulting electrostatic potentials. For modeling, we considered different modes of ion transport using the Nernst-Planck equation for the transport of dilute species coupled with the Poisson-Boltzmann equation for the equilibrium distribution of ions. To perform these calculations, however, we must first identify an equivalent simplified geometry using the approach described in our prior work². The cross-section of the simulated axis-symmetric geometry is shown below. The mesh elements are shown, where we have used a boundary elements mesh close to the liquid-solid boundary.

Governing equations:

$$\nabla \cdot J_i + U \cdot \nabla c_i = 0 \quad (S16.1)$$

$$J_i = -D\nabla c_i - z_i \mu_i^m F c_i \nabla \Phi \quad (S16.2)$$

$$\nabla^2 \Phi = -\frac{1}{\epsilon_0 \epsilon_r} \sum_i F z_i c_i \exp\left(-\frac{e z_i \Phi}{k_B T_S}\right) \quad (S16.3)$$

We used surface charge density as the boundary condition, which is not a fixed value but is instead governed by the above equilibrium reaction²⁻⁴. This results in variable surface charge density that depends on the surface potential at the stern plane, given by the following equation:

$$\sigma = \frac{-e\Gamma}{1 + \frac{[H^+]_S}{K_a}}, \text{ and} \quad (S16.4)$$

$$[H^+]_S = [H^+]_{bulk} \exp\left(-\frac{e\Phi_S}{k_B T_S}\right) \quad (S16.5)$$

The material's chemical characteristic Δ_H is the enthalpy of dissociation of the surface groups. Then, we swept Δ_H , and obtained voltage-temperature lines for various conditions. This enabled us to obtain the open circuit voltage (surface charge) as a function temperature for various conditions, such as by varying electrolyte concentration, pH, and K_{a0} . Finally, we constructed the correlation between the slopes of voltage-temperature lines and their value Δ_H .

$$K_a = K_{a0} \exp \left[-\frac{\Delta_H}{R} \left(\frac{1}{T} - \frac{1}{T_0} \right) \right] \quad (S16.6)$$

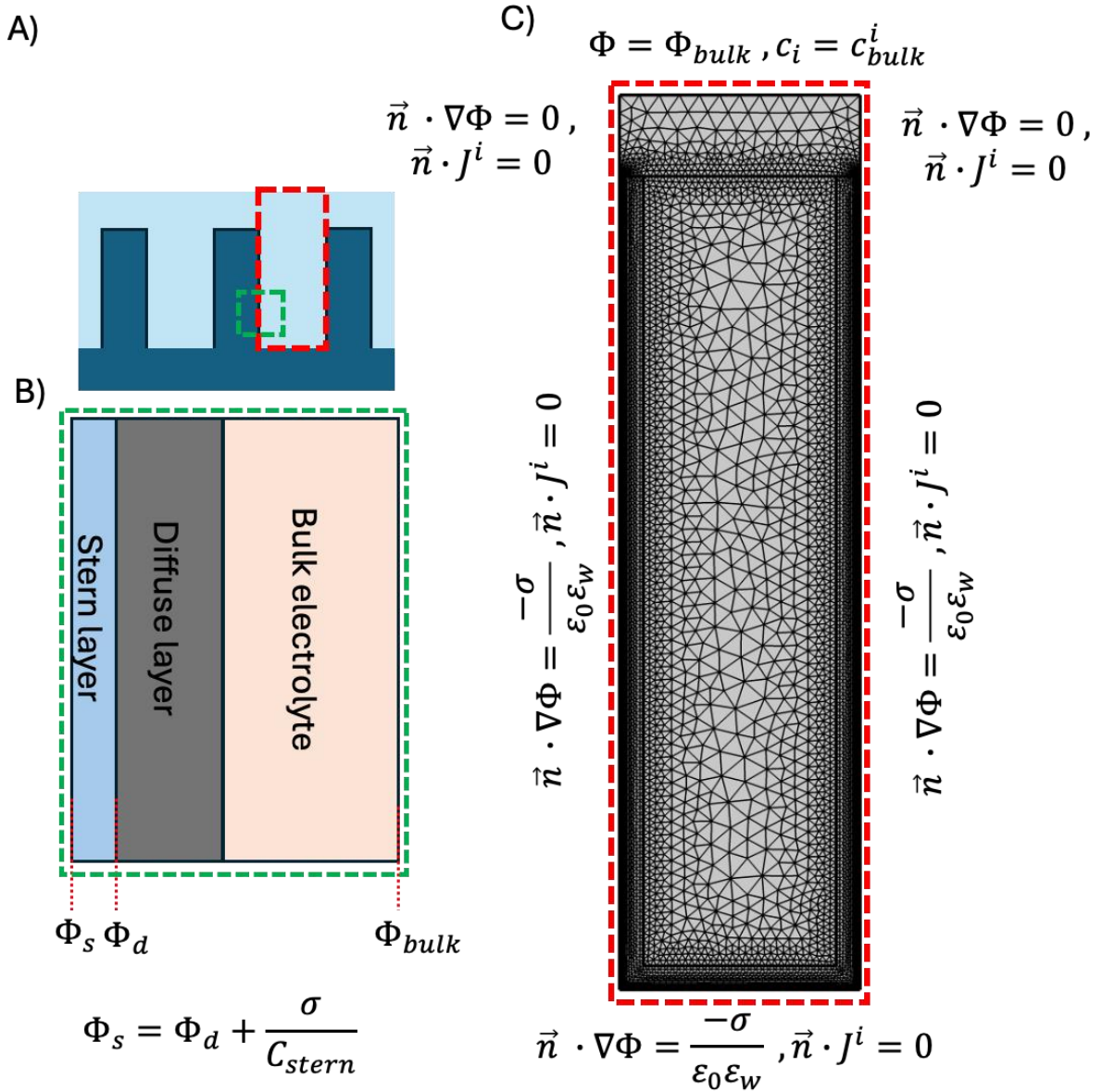


Figure S16: **A)** Cross-section of the device's nanostructure with the region where the governing equations are solved (enclosed in red rectangle). **B)** Zoom-in view of the liquid-solid interface (shown in a green rectangle) with the potential at the stern plane and diffuse layer. The equation gives the relation between the potential at the stern and diffuse layer connected by the surface charge density and stern layer capacitance. **C)** Cross-section the simplified axis-symmetric geometry used in the numerical simulation

after building the mesh. The boundary conditions for the electrical potential and ion flux are shown at different boundaries.

Table S16: Value of the parameters used in the simulation.

T₀	298.1 K	Ambient temperature
t_{stern}	0.5 nm	Stern layer thickness
pH_b	7	pH of bulk electrolyte
V_{therm}	$k_B T / q$	Thermal voltage
W_{Ag}	4.6 V	Work function of Ag
E_{eq}	0.2 V	Equilibrium potential of reference electrode
D_A	1e-9 m ² /s	Diffusion coefficient, cation
D_X	1e-9 m ² /s	Diffusion coefficient, anion
D_H	36.3e-4[cm ² /(Vs)]*V _{therm}	Diffusion coefficient, H+
D_{OH}	20.5e-4[cm ² /(Vs)]*V _{therm}	Diffusion coefficient, OH-
C₀	0.001 M	Bulk electrolyte concentration
cH_{bulk}	10 ^{-pH_b} M	Bulk H+ concentration
cOH_{bulk}	10 ⁻¹⁴ [M ²]/cH _{bulk}	Bulk OH- concentration
cA_{bulk}	c ₀ +cOH _{bulk}	Bulk cation concentration
cX_{bulk}	c ₀ +cH _{bulk}	Bulk anion concentration
z_A	1	Cation charge
z_X	-1	Anion charge

I_{bulk}	$0.5 * (z_A^{2*} c_{A_{bulk}} + z_X^{2*} c_{X_{bulk}} + c_{OH_{bulk}} + c_{H_{bulk}})$	Bulk ionic strength
ϵ_w	78.5	Relative permittivity of water
F	96485 C/mol	Faraday's constant
R	8.3145 J/mol.K	Universal gas constant
λ_D	$\sqrt{\frac{\epsilon_0 \epsilon_w V_{therm}}{2F I_{bulk}}}$	Debye length
ϵ_{st}	12	Relative permittivity of Stern layer
C_{st}	$\frac{\epsilon_0 \epsilon_w}{t_s}$	Stern layer capacitance
K_{a0}	$10^{-pK_{a0}}$ M	Equilibrium constant
Γ	8×10^{14} 1/cm ²	Oxide surface binding site density
Φ_{bulk}	$-W_{Ag^-} - E_{eq}$	Bulk electrical potential
t_w	0.1 μ m	Thickness of water layer
K_a	$K_{a0} \exp\left[-\frac{\Delta_H}{R} \left(\frac{1}{T} - \frac{1}{T_0}\right)\right]$	Equilibrium constant at temperature T
Δ_H	50 kJ/mol	Enthalpy of dissociation
pK_{a0}	6	Equilibrium constant at ambient temperature

References

1. Sposito, G. On the surface complexation model of the oxide-aqueous solution interface. *Journal of Colloid and Interface Science* **91**, 329–340 (1983).
2. Anwar, T. & Tagliabue, G. Salinity-dependent interfacial phenomena toward hydrovoltaic device optimization. *Device* **2**, 100287 (2024).
3. Behrens, S. H. & Grier, D. G. The charge of glass and silica surfaces. *The Journal of Chemical Physics* **115**, 6716–6721 (2001).
4. Stein, D., Kruithof, M. & Dekker, C. Surface-Charge-Governed Ion Transport in Nanofluidic Channels. *Phys. Rev. Lett.* **93**, 035901 (2004).